RICE UNIVERSITY

Smart Cantilever Beams for Nanomanipulation

by

Yan Chen

A THESIS SUBMITTED
IN PARTIAL FULFILLMENT OF THE
REQUIREMENTS FOR THE DEGREE

Master of Science

APPROVED, THESIS COMMITTEE:

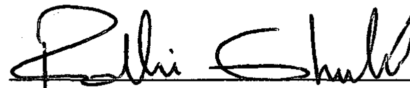

Dr. Fathi H. Ghorbel, Chair
Professor of Mechanical Engineering and Materials Science

Dr. Marcia K. O'Malley
Assistant Professor of Mechanical Engineering and Materials Science

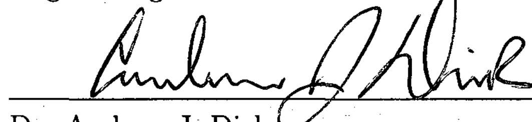

Dr. Andrew J. Dick
Assistant Professor of Mechanical Engineering and Materials Science

HOUSTON, TEXAS

APRIL, 2009

UMI Number: 1466767

INFORMATION TO USERS

The quality of this reproduction is dependent upon the quality of the copy submitted. Broken or indistinct print, colored or poor quality illustrations and photographs, print bleed-through, substandard margins, and improper alignment can adversely affect reproduction.
In the unlikely event that the author did not send a complete manuscript and there are missing pages, these will be noted. Also, if unauthorized copyright material had to be removed, a note will indicate the deletion.

UMI®

UMI Microform 1466767
Copyright 2009 by ProQuest LLC
All rights reserved. This microform edition is protected against unauthorized copying under Title 17, United States Code.

ProQuest LLC
789 East Eisenhower Parkway
P.O. Box 1346
Ann Arbor, MI 48106-1346

Abstract

Smart Cantilever Beams for Nanomanipulation

by

Yan Chen

A smart micro cantilever beam, consisting of an atomic force microscope probe bonded with a piezoelectric actuator, is proposed to enhance the ability of mechanical nanomanipulation. A precise three-section Euler-Bernoulli beam model is developed to describe the dynamics of the beam. The forced vibration solution of this model with respect to two independent inputs from the piezoelectric actuator and the base excitation is derived. Through the solution and the geometry relationship, the trajectory of the end of the tip is obtained from the motion of the free end of the AFM probe. Based on the resonant response from two harmonic inputs, nano-scale elliptical and linear tip trajectories are predicted at the second dynamic mode. Analytical and numerical studies show that the characteristics of the resulting trajectories are influenced by the magnitudes of the two inputs. The potential applications of the elliptical and linear trajectories for nanomanipulation are proposed.

Acknowledgements

I dedicate this work to my parents Li, Ya Zhong and Chen, Ji Ying and my brother Li, Man Lu.

I would like to express my gratitude to my advisor, Dr. Fathi Ghorbel, who has been my mentor and my guide. His support and guidance were invaluable to the success of my efforts. I would like to thank Dr. Andrew Dick for his helpful suggestions and comments from time to time. I would also like to thank Dr. Marcia O'Malley, for being helpful and accommodating throughout the process of the defense of this work.

Thanks to my colleagues and friends, Sushant M. Dutta, Fakhri Landolsi, and Andrew Lynch, for their help and camaraderie throughout. Many thanks go to Lu, Hao for discussion on atomic force microscope systems and related experiments. Thanks to my roommates Liu, Kai Jiang and Hu, Bei and Zhang, Zhi for meaningful discussion on mathematical knowledge.

Finally, thanks to all my family and friends, who have been my pillars of strength through thick and thin.

Table of Contents

Abstract ii

Acknowledgements iii

List of Figures vii

List of Tables viii

1 Introduction 1

1.1 Nanomanipulation 2

1.2 Piezoelectric Materials and their Applications 7

1.3 Designs of Smart Micro Cantilever Beams 10

1.4 Outline of this Thesis 13

2 Mathematical Modeling of the Smart Micro Cantilever Beam 15

2.1 Configuration of the Smart Micro Cantilever Beam 15

2.2 Mechanical Models of the Piezoelectric Actuator 16

2.3 Dynamic Model of the Smart Micro Cantilever Beam 21

2.4 Discussion 27

3 Tip Trajectory Characterization 29

3.1 Tip Trajectory Derivation 29

3.2 Characterization 33

4 Simulation Results and Discussion 36

4.1 Elliptical and Linear Tip Trajectory 36

4.2 Applications in Nanomanipulation 43

4.3 Discussion 45

5 Conclusions **46**

Bibliography **52**

List of Figures

1.1 Categories of nanomanipulation approaches [46, 15] 4

1.2 Basic structure of nanomanipulation systems [46] 6

1.3 Frequency response of the first and the second modes 11

1.4 Forced response of a cantilever beam 12

1.5 The distribution of Young's modulus 13

2.1 The configuration of the smart micro cantilever beam. 16

2.2 The induced stress of the piezoelectric actuator. 17

2.3 Strain distribution in the simple block force model 18

2.4 Strain distribution in the uniform strain model 18

2.5 Strain distribution in the Bernoulli-Euler model 19

2.6 The configuration of the smart micro cantilever beam with two stepped variations on the geometry, materials and induced moment. 21

3.1 The profile of the modal solution at the second eigenmode and the profile of the special solution when $Y_0 = 2$ nm and $V_0 = 1$ volt. 30

3.2 The geometry relationship between the free end of the smart micro cantilever beam and the end of the tip. 31

3.3 An elliptical trajectory of the end of the tip with the semiminor axis a, the semimajor axis b and the rotation angle θ. 34

4.1 The variation of the rotation angle with different input ratios and tip lengths. 38

4.2 The trends of tip trajectories corresponding to different inputs. 39

4.3 The variation of the semiminor axis (solid line) and semimajor axis (dashed line) with continuous increase of Y_0. 40

4.4 The variation of the semiminor axis (solid line) and semimajor axis (dashed line) with continuous increase of V_0. 41

4.5 Potential applications of resulting trajectories on three-dimensional nanomanipulation. In application I and II, the side portion and bottom portion of an elliptical trajectory can be used to machine a curved plane and a nano-trench, respectively. While a linear trajectory can be applied to shape an inclined plane in application III. 44

List of Tables

4.1 Parameters for simulation. 37

4.2 The trends of tip trajectories. 42

Chapter 1

Introduction

Nanomanipulation, one important area in nanotechnology, has attracted more and more attention recently [46, 15, 48, 53, 52, 41]. Chronologically, nanomanipulation examples on positioning atoms were first reported in the late 1980s [5, 17, 16], which usually happened in a scanning tunnelling microscope (STM) system at a very low temperature. Along with the development of microscopy, other instruments, such as the Zyvex S100 system and atomic force microscope (AFM) system, have also been applied to push nano-spheres [34] and nano-wires [53].

Although manipulation of nano-scale objects has been realized for almost twenty years, there are a variety of definitions of nanomanipulation in the nanotechnology community. Thus, different definitions of nanomanipulation are first discussed in Section 1.1. A general definition of nanomanipulation is proposed and applied to explain the relationship between nanomanufacturing and nanomachining. Next, different approaches and the main tools of nanomanipulation are introduced. Mechanical nanomanipulation as one important approach is emphasized and the basic configuration of a mechanical nanomanipulation system is discussed. In the basic configuration, a micro-scale cantilever beam structure is introduced as one key component to directly interact with nano-objects.

Section 1.2 presents how smart materials, like piezoelectric materials, can be applied to modify a micro-cantilever beam structure. Thus, the so-called smart micro cantilever beam is expected to generate new dynamics due to the introduction of smart materials. The resulting new dynamics of the smart micro cantilever beam are anticipated to be used in new nanomanipulation tasks. Following this idea, three different approaches are

explored to develop smart micro cantilever beams with smart materials in Section 1.3. The main results and feasibility of each approach are discussed. Finally, the outline of this thesis is shown in Section 1.4.

1.1 Nanomanipulation

In order to identify the scope of research in the area of nanomanipulation, the definition of nanomanipulation must be specified first. However, although the first nanomanipulation example was reported twenty year ago [5], there is no agreement in the literature regarding the definition of nanomanipulation.

One definition of nanomanipulation was proposed as the manipulation of nanometer size objects with a nanometer size end-effector with (sub)nanometer precision [46]. In this definition, the object, method and requirement of nanomanipulation are contained. However, the utility of a nanometer size end-effector is not necessary for nanomanipulation since many chemical and physical methods are applied in nanomanipulation without a physical end-effector. For example, an electric field was used to achieve nanomanipulation in order to assemble nano-scale objects [45].

Another definition of nanomanipulation is given [1]: the process of manipulating items at an atomic or molecular scale in order to produce precise structures. In this definition, the object and purpose of nanomanipulation are identified. However, the aim of nanomanipulation must be discussed further. Many nanomanipulation procedures are designed for the test of mechanical characteristics of nano-scale materials, which do not necessarily lead to precise structures. For example, if mechanical characteristics of a nano-wire need to be measured, the first step is to pick up one nano-wire from a lot of nano-wire samples effectively and quickly, and then accurately position the nano-wire for testing. During this challenging process, no new structure is produced.

Based on the existing definitions, a more general definition of nanomanipulation is proposed in this thesis: nanomanipulation is a process in which nano-scale objects are

manipulated by controlled external forces or mechanisms with (sub)nanometer precision. In this definition, the object, method and requirement of nanomanipulation are contained. All the chemical, physical and biological methods are included in this definition. The process not the purpose of nanomanipulation is emphasized since nanomanipulation may not have an obvious aim to achieve comparing with nanomanufacturing. Furthermore, this definition also clearly distinguishes nanomanipulation from two other important concepts, nanomanufacturing and nanomachining.

Nanomanufacturing as a higher level concept was defined as all processes aimed toward building of nanoscale (in 1D, 2D or 3D) structures, features, devices, and systems suitable for integration across higher dimensional scales (micro-, meso- and macroscale) to provide functional products and useful services [7]. From this definition, it is clear that nanomanufacturing emphasizes nano-scale devices and systems with certain function, which does not need to be satisfied in the process of nanomanipulation. Nanomanufacturing is a systematical concept which requires more complicated tools and processes. The progress and vigorousness of nanomanufacturing is based on accurate, quick, integrated and automatic nanomanipulation. Recent progress and examples in nanomanufacturing can be found [14]. Nanomachining involves changing the structure of nano-scale materials and usually portions of the nano-structure are removed or modified [1]. From this definition, nanomachining can be regarded as a subset of nanomanipulation which emphasizes structure change. One example on nanomachining is the action of indenting sample surface in nanolithography [28].

From the discussion above, nanomachining is able to be considered as a special case of nanomanipulation, which is the basis of nanomanufacturing. Therefore, although nanomanipulation usually involves simple actions such as pushing or pulling, cutting, picking and placing, positioning, orienting, indenting, bending, rubbing, twisting and assembling, this field is one key component of nanotechnology. Next, the main approaches and tools adopted in nanomanipulation will be introduced .

According to different criteria, the approaches of nanomanipulation are classified into

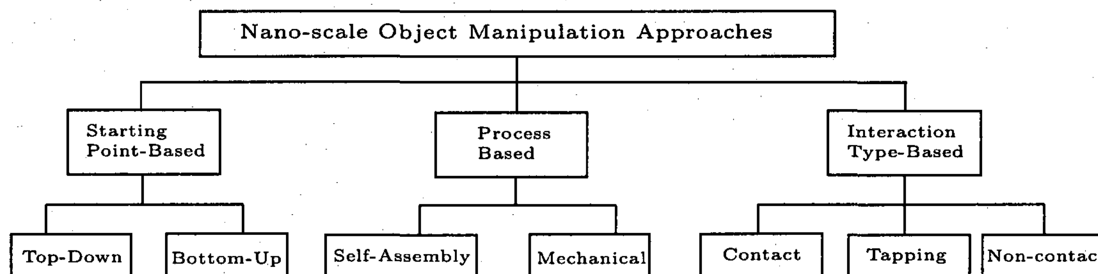

Figure 1.1: Categories of nanomanipulation approaches [46, 15]

different categories shown in Figure 1.1, which is modified from [46, 15]. Two main approaches, top-down and bottom-up, are classified based on different starting points. The top-down approach involves the creation of nano-scale objects from a parent entity that is larger. The trend of action is from large scale to small scale. On the other hand, the bottom-up method involves the process of building bigger and more complicated structures from nano-scale particles. The trend of action is from small scale to large scale. From the criterion of interaction type, three different approaches are displayed in Figure 1.1. With the contact approach, the manipulator and the object keep contact during nanomanipulation. The manipulator intermittently makes contact with the object of interest to achieve nanomanipulation when using the tapping approach. For the non-contact approach, non-contact forces, such as magnetic forces and repulsive forces, are utilized during nanomanipulation. Typically, the AFM system is a standard tool which works under these three different working modes [38, 13, 42].

Another important classification is based on the process involved in nanomanipulation. Two different categorizes, directly self-assembly and mechanical nanomanipulation, are illustrated in Figure 1.1. The directly self-assembly approach assembles bigger and more complicated structures from nano-scale particles by using chemical or biological mechanisms. On the other hand, the mechanical approach manipulates nano-scale objects with micro-scale end-effectors which is mainly based on various kinds of microscopes. The mechanical nanomanipulation is important because this approach has a strong connec-

tion with other methods. For example, since micro-scale end-effectors in microscopes are adopted, all the interaction ways, such as contact, tapping and non-contact, can appear in the mechanical approach.

From the discussion above, the mechanical method as one of the important nanomanipulation approaches is mainly based on different kinds of scanning probe microscopes. Many examples were reported since physicists and engineers created different types of microscopes to adopt this approach. In early work, STM was used to position nano-scale particles [5, 17]. Individual physisorbed atoms were fully controlled by STM to perform positioning tasks [16]. Later, nanomanipulation tasks were successfully accomplished by using AFM systems. Junno et al. first realized fully controlled positioning of nanometer-sized objects by using AFM [25]. Hansen et al. adopted an imaging-pushing-imaging scheme in controlled pushing of a nano-scale particle [21]. AFM was switched between the tapping mode and the contact mode to fulfill a simple and easy nanomanipulation. Resch et al. showed that the nano-scale particles were pushed along the surface once a critical contact force between tip and gold cluster was exceeded [40]. In addition, the average separation between the tip apex and the sample was estimated.

While providing initial nanomanipulation capabilities, individual microscope like STM and AFM, cannot satisfy some requirements on nanomanipulation, such as real-time monitoring of manipulation. Thus, hybrid nanomanipulation systems produced by integrating functions of multiple microscopes were proposed. For example, since scanning electron microscope/transmission electron microscope (SEM/TEM) can offer real-time vision, a piezotube driven nanomanipulator was equipped inside the specimen holder of TEM for nanomanipulation [27, 12]. A system integrating SEM with AFM was used to test mechanical properties of nanotubes via bending, translating and rotating via online observation [20, 50]. Another new nanomanipulation system combining AFM and SEM with improvement in variable viewing angle of the contact point between the AFM tip and the sample was discussed recently [18].

Although hybrid microscopes were created for various nanomanipulation, AFM-based

nanomanipulation systems have some significant advantages comparing with other microscopes. For example, an AFM system can function in an atmospheric environment at room temperature, while STM can only work in a vacuum environment at a very low temperature. SEM and TEM are also limited by a vacuum working environment. Furthermore, samples used in an AFM system could be conductive or nonconductive, solid or liquid, thick or thin and get no strict limitation. While conductive samples have to be used in STM and no liquid samples can be used in SEM and TEM. Thus, most biological samples which usually contain liquid can be only used in AFM-based systems but not in other microscopes. In view of the importance of AFM-based nanomanipulation systems, a basic structure which is used in mechanical nanomanipulation is illustrated in Figure 1.2 [46, 47].

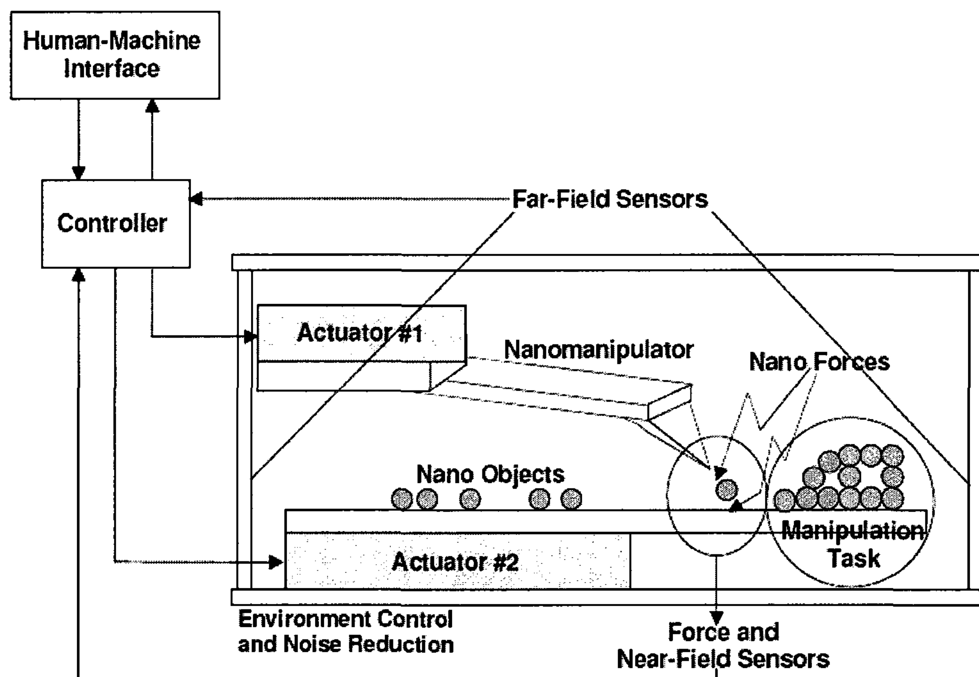

Figure 1.2: Basic structure of nanomanipulation systems [46]

The main parts of a AFM-based nanomanipulation system are nanomanipulators, actuators, sensors and controllers, as shown in Figure 1.2, which are similar to a macro-scale control system. One key component is the micro-scale cantilever beam with a tip at the free end which is used as a nanomanipulator. Since the tip located at the free end of the

micro-scale cantilever beam directly interacts with the samples during manipulation, the dynamics of the tip and the corresponding dynamics of the micro-scale cantilever beam are important for fulfilling nanomanipulation tasks.

Based on differently dynamic characteristics of the micro-scale cantilever beam, two main categories are usually classified: the nonvibrating-cantilever nanomanipulation and the vibrating-cantilever nanomanipulation. The former one means that the cantilever, which is used as a rigid end effector, does not vibrate during nanomanipulation. Tasks like positioning, pulling or pushing were fulfilled by a nonvibrating-cantilever [25, 21, 40]. On the other hand, a vibrating cantilever beam was also used in nanomanipulation, especially with respect to nanomachining. Klehn and Kunze adopted the vertical motion of the tip at the first mode of the cantilever beam to perform a nanolithography technique [28]. Recently, the horizontal motion of the end of the tip at the second dynamic mode of a concentrated-mass cantilever was used to rub soft sample materials [36, 35].

From the discussion above, it can be seen that knowledge of the dynamics of the micro-scale cantilever beam and the corresponding trajectories of the tip in an AFM-based system are crucial for nanomanipulation. Different dynamics of the micro-scale cantilever beam can be used for different nanomanipulation tasks. Thus, in order to enhance the ability of nanomanipulation, methods for producing other complex movements with the micro-scale cantilever beam need to be considered. A feasible way of applying smart materials to the micro-scale cantilever beam is discussed in next section.

1.2 Piezoelectric Materials and their Applications

From the discussion in Section 1.1, the tip trajectory of a micro-cantilever beam in a AFM-based system is determined to be important in nanomanipulation. Since the tip trajectory is directly dependent on the dynamics of the micro-cantilever beam, a method to modify the dynamics of the micro-cantilever beam is necessary for enhancing the capabilities of nanomanipulation. The idea of applying smart materials to change the dynamics of a

micro-scale beam structure can be inspired by research on macro-scale systems.

Piezoelectrics, one of the most popular smart materials, are being widely utilized in sensors and actuators due to their capability of exchanging mechanical energy with electrical energy, see [10] and references therein. For piezoelectric materials, strain is produced when a voltage is applied:

$$\varepsilon_p = \frac{d_{31}}{h_p} V(x,t) \tag{1.1}$$

where d_{31} is the electric charge constant, h_p is the thickness of piezoelectric materials and $V(x,t)$ is the applied voltage. Thus, the stress due to the strain is expressed based on the Hooke's Law.

$$\sigma_p = E_p \varepsilon_p \tag{1.2}$$

where E_p is the Young's modulus of piezoelectric materials. Furthermore, the resulting force is considered as

$$F_p = A_p \sigma_p \tag{1.3}$$

where A_p is the cross area of piezoelectric materials. Formulas (1.1)-(1.3) express the process of producing a force from a voltage signal when piezoelectric materials are applied in actuators. In reverse, when piezoelectric materials are applied in sensors, a voltage signal can be produced from external forces since these formulas are reversible.

In many applications, piezoelectric patches or layers were adhesively bonded to existing systems as distributed actuators and sensors to build smart structures [37]. A smart beam structure, which is formed by attaching piezoelectric materials to a host beam, has been studied extensively. Early smart beam structures appeared in space systems. Piezoelectric actuators were applied to attenuate the vibration of a satellite structure [4] and control the shape of antenna reflectors on satellites [3]. Similar structures were expanded to airplane wings and helicopter blades, in which piezoelectric patches were adopted for flutter suppression [29] and gust alleviation [9], respectively. Recently, vibration control of smart beam structures was applied to a macro-scale manipulator bonded with piezostack actuators [26].

In recent years, smart beam structures have been extended to micro scales along with the development of AFM systems. An AFM probe, typically represented by a micro-cantilever beam mounted with a perpendicular tip at the free end [6], is the main host structure to compose smart micro cantilever beams in many applications. In the tapping mode for nanoimaging, AFM probes were excited by bonded piezoelectric-layer actuators to improve the imaging speed beyond the capabilities of conventional base-excitations from piezotubes which had lower bandwidths [30, 49]. In the case of nanomanipulation, when an AFM probe was adopted to reliably push a nanowire with its tip, the probe was made stiffer and maintained straight by the attached piezoelectric layer to avoid slipping over the object [53]. Moreover, when AFM probes were used for sensing, attached piezoelectric layers enabled the probes to detect chemical gas [2] and ultra small mass [19] with the characteristics of self-sensing and self-actuating.

Examples shown above presents a potential way to modify the AFM probe with piezoelectric materials. However, these applications were not focused on actively adjusting tip trajectories of the AFM probe for nanomanipulation. Some researchers have studied the tip trajectories and related applications without using a smart micro cantilever beam. By using the vertical trajectory at the first dynamic mode, Klehn and Kunze [28] adopted a common AFM probe to plastically indent a thin resist layer on the sample surface. This dynamic plowing process to mold a mask for subsequent wet-chemical etching displayed an alternative low-cost and low-effort nanolithography as compared with the high-resolution electron-beam technique. In order to enhance the machining quality, Muraoka et al. [36, 35] proposed a new nano-scale rubbing process consisting of material removal rather than plastic deformation in dynamic plowing. When a concentrated-mass (CM) probe, an AFM probe with a concentrated mass at the free end, was vibrated at the second dynamic mode, the end of the tip was used to horizontally scratch the sample surface due to a new node produced at the end of the CM probe. In these applications, the linear trajectories of the probe tip depended entirely on the structure of the cantilever beam were used to accomplish the nanomachining tasks. However, when more complicated

processes are required, such as machining a nano-scale curved surface, these methods are not sufficient. Thus, in order to improve the ability of nanomanipulation, other flexible tip trajectories need to be created by new techniques.

1.3 Designs of Smart Micro Cantilever Beams

The idea of applying smart materials to the AFM probe is discussed in this section. Three main methods to modify the dynamics of the AFM probe are examined. The main results and limitations in the firt two methods are presented. The third feasible way is selected as an effective design and will be discussed in detail.

Since tip trajectories can not be directly designed, the dynamics of an AFM probe is examined when piezoelectric material is applied. It is meaningful to study the dynamic vibration of an AFM probe. First of all, the most popular dynamic method used in AFM, the tapping mode, is based on the vibrations of the AFM probe. Thus, it is easy to utilize some existing setups of AFM systems for nanomanipulation. On the other hand, it is an ideal situation if a smart micro cantilever beam for nanomanipulation is also able to image the result under the tapping mode. Secondly, for nanomanipulation, especially in nanomachining, the mode shapes of the cantilever give us a stable, repeatable and well-defined motion of the tip with enough manipulation force or moments. Thirdly, the dynamics of cantilever attracts more and more attention recently, not only on the vertical bending modes but also on lateral bending modes and torsion modes [39]. All these dynamic modes give us potential methods to build a smart micro cantilever beam for nanomanipulation.

Although the dynamic response of an AFM probe is closely related to physical properties such as density, area moment of inertia and Young's modulus, the external factors can also influence the motion of the probe. Thus, the modification of the mode shapes by introducing external forces and moments is first considered.

The first method introduces a base excitation to the micro cantilever beam from one

piezoelectric actuator. Based on the Euler-Bernoulli model, a special forced response of a micro smart cantilever beam is designed. A node is produced at the free end of the cantilever beam by combining the first and second mode response. An excitation frequency between the first eigenfrequency and the second eigenfrequency is obtained via frequency design, as shown in Figure 1.3. The spatial profile of the forced response displaying the end of the cantilever as a node is shown in Figure 1.4. The whole cantilever beam vibrate around the balance position. This is similar to the result of a CM cantilever beam [35]. However, the amplitude is very small in Figure 1.4. At the excitation frequency, the magnitude of the whole cantilever beam is around one thousandth of the magnitude at the first eigenfrequency from Figure 1.3. This may lead to problems of sensing in AFM since the sensitivity of the laser reflection is dependent on the slope at the tip which is associated with the change of amplitudes. Thus, this method has limitations regarding its application to nanomanipulation.

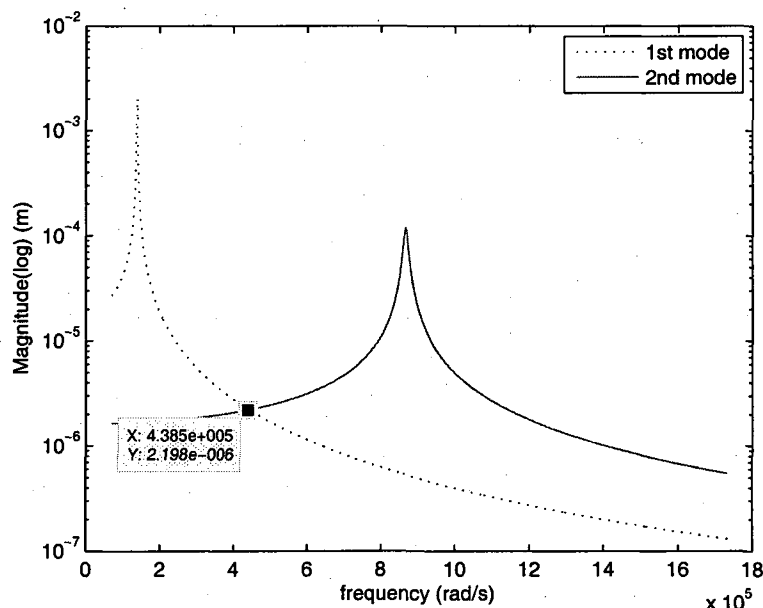

Figure 1.3: Frequency response of the first and the second modes

The second method consists of developing a cantilever beam with a non-uniform Young's

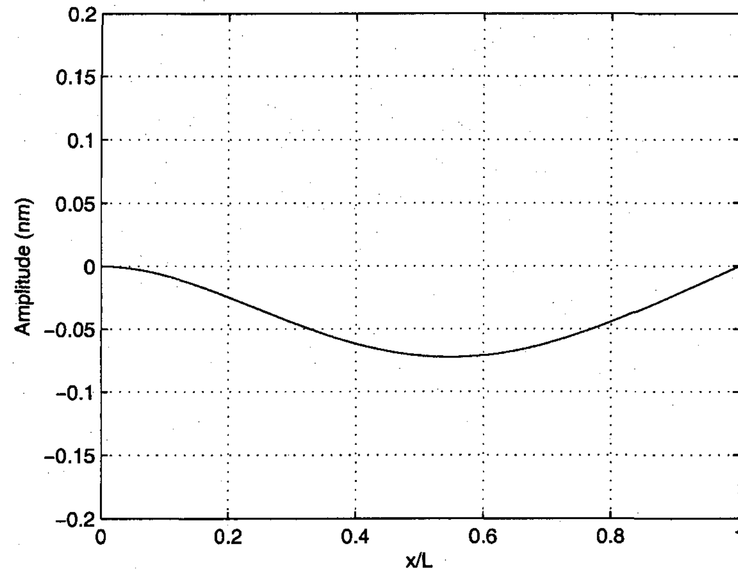

Figure 1.4: Forced response of a cantilever beam

modulus. A special non-uniform beam with varied effective bending stiffness is designed via the method of finite element analysis. As shown in Figure 1.5, this distribution of the Young's modulus results in an approximate node at the free end of the cantilever beam, which has the similar effect as a CM cantilever beam [35]. Although finite element analysis is a effective method to analyze this design problem, the practical distribution of the Young's modulus is difficult to achieve as the finite element design since the distribution is continuous and not discrete.

The third method utilizes a bonded piezoelectric actuator on the micro cantilever beam. Different from the first method by introducing a base excitation, the dynamic influence from a bonded piezoelectric actuator exhibits new features. Furthermore, combining with the base excitation, new dynamics of the cantilever beam and consequently varying tip trajectories are achieved. The application of two independent inputs has advantages on adjusting the dynamics of the cantilever beam *in situ*. This approach is also more practical than modifying the Young's modulus of the beam with finite element design since piezoelectric actuators have already been widely applied to the AFM probes. Thus, this

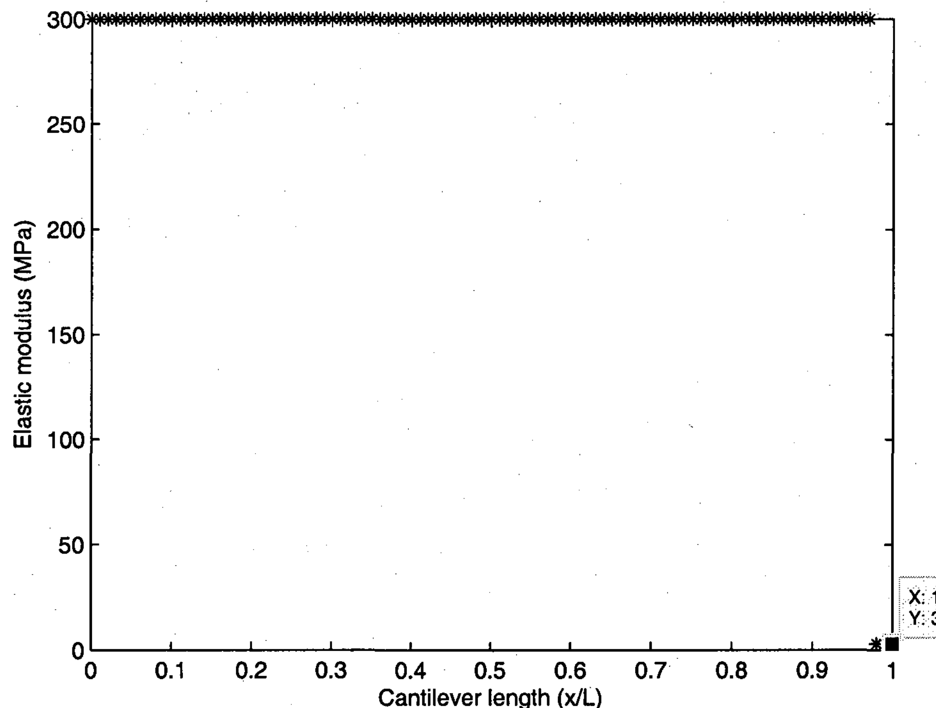

Figure 1.5: The distribution of Young's modulus

method is selected as an effective design and will be discussed in detail in the remainder of this thesis.

1.4 Outline of this Thesis

The remainder of this thesis is organized as follows. In Chapter 2, a segmented Euler-Bernoulli beam model including two inputs is developed and a forced response is derived for a smart micro cantilever beam with piece-wise varying geometry and materials. The tip trajectory is derived from the motion of the free end of the cantilever beam based on its geometric relationship with the probe tip in Chapter 3. Simulation results and discussion on elliptical and linear tip trajectories are presented in Chapter 4. According to the resulting tip trajectories, three potential implementations of these trajectories for

AFM-based nanomanipulation are proposed. Chapter 5 presents the conclusions of this thesis.

Chapter 2

Mathematical Modeling of the Smart Micro Cantilever Beam

The importance of modeling the smart micro-cantilever beam to obtain the motion of the free end, and consequently the tip trajectories has already been motivated in Chapter 1. In this chapter, a complete and precise mathematical model is developed to describe the dynamic response of the smart micro cantilever beam. Section 2.1 first introduces the basic configuration of the smart micro cantilever beam. Different mechanical models to explain how the piezoelectric actuator influence the micro-scale cantilever beam are summarized and discussed in Section 2.2. The Bernoulli-Euler model is selected as the most suitable model and used for the dynamic analysis. In Section 2.3, a three-segmented Euler-Bernoulli beam model is developed to describe the dynamics of the smart micro cantilever beam with piece-wise linear properties. Furthermore, the forced vibration solution of this model with respect to two independent inputs from the piezoelectric actuator and the base excitation is derived. A significant contribution of this work is the solution of the model presented in this chapter which differs from previous works and is believed to be more accurate. The new part of the solution, which is only related to the piezoelectric actuator, is necessary to produce various tip trajectories.

2.1 Configuration of the Smart Micro Cantilever Beam

The smart micro cantilever beam, consisting of a micro-cantilever beam bonded with a piezoelectric patch, is shown in Figure 2.1. Since the tip located at the free end of the

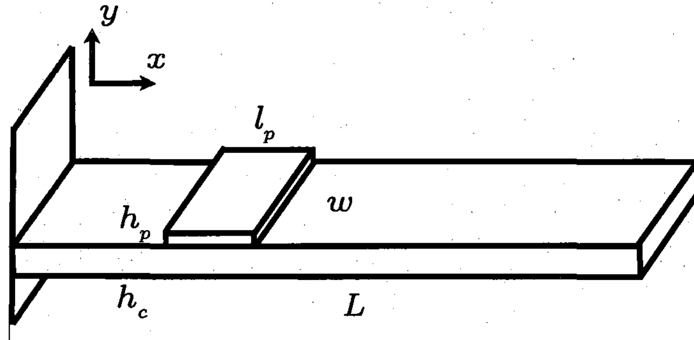

Figure 2.1: The configuration of the smart micro cantilever beam.

smart micro cantilever beam does not influence the mechanical analysis, it is not plotted in Figure 2.1. The parameters L, h_c and l_p, h_p represent the length and thickness of the cantilever beam and the piezoelectric patch, respectively. Without loss of generality, it is assumed that the cantilever beam and the piezoelectric actuator have the same width w.

Unlike a nonuniform beam with variable cross-sectional area, the surface-bonded piezoelectric patch introduces extra strains and stresses as well as nonuniform geometry and materials to the micro cantilever beam. Thus, a precise mathematical model should consider influences from both induced strains and nonuniformities. Since the influence of the strains and stresses introduced by the piezoelectric actuator is a basis on which the dynamic model relies, the mechanical models of the piezoelectric actuator are first discussed in Section 2.2. The property of nonuniform geometry and materials will be considered when the dynamic model of the smart micro cantilever beam is derived in Section 2.3.

2.2 Mechanical Models of the Piezoelectric Actuator

When a voltage $V(x,t)$ is applied to create an electric field across piezoelectric materials, the induced strain is generated within the piezoelectric patch due to the converse piezoelectric effect, as shown in equation (2.1).

$$\varepsilon_p = \frac{d_{31}}{h_p} V(x,t) \tag{2.1}$$

where d_{31} is the electric charge constant, h_p is the thickness of the piezoelectric actuator and $V(x,t)$ is the applied voltage. So the stress due to the strain are expressed in equation (2.2) according to the Hooke's Law.

$$\sigma_p = E_p \varepsilon_p \tag{2.2}$$

where E_p is the Young's module of the piezoelectric actuator. Thus, a stress introduced in the piezoelectric actuator in the direction of the x axis is shown in Figure 2.2.

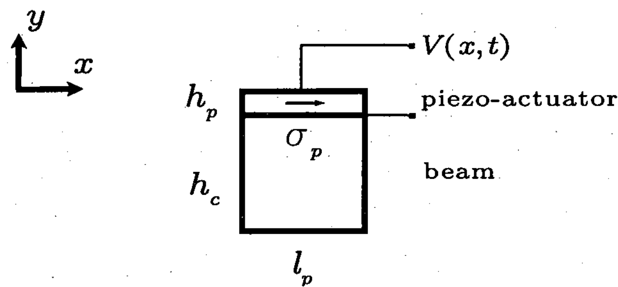

Figure 2.2: The induced stress of the piezoelectric actuator.

As shown in Figure 2.2, the unique induced strain and stress from the piezoelectric actuator is obtained based on the property of piezoelectric material. However, there are different models to explain how the induced strain and stress transfer to the beam structure. These different models are summarized and discussed in the following.

1. The Simple Blocked Force Model

   In the simple blocked force model, which was also referred to as the pin-force model [8], the actuator is idealized as a line force source applied to the structure. A perfect transfer of strain is assumed between the piezoelectric actuator and the surface of the cantilever beam to which it is bonded. The distribution of the strains across the composite portion is illustrated in Figure 2.3.

2. The Uniform Strain Model

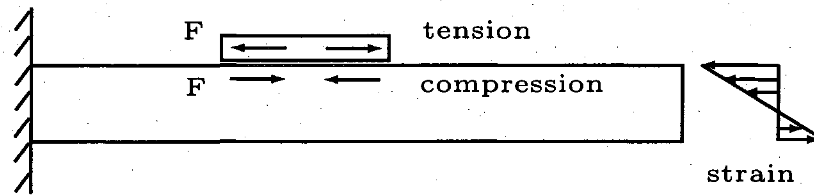

Figure 2.3: Strain distribution in the simple block force model

In the uniform strain model, the so-called shear lag phenomenon is considered on the basis of the simple blocked force model, which means that some of the strain generated by the piezoelectric actuator is dissipated in the deformation of the bond layer itself due to the finite stiffness of the bond layer. The bond layer is assumed to undergo pure shear deformation. The distribution of the strains across the composite portion is illustrated in Figure 2.4.

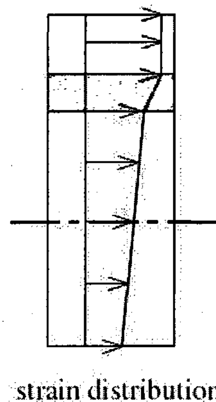

Figure 2.4: Strain distribution in the uniform strain model

3. The Bernoulli-Euler Model

In the Bernoulli-Euler model, the beam and piezoelectric actuator are considered as a continuous structure and a linear strain is distributed in the cross-section for both the actuator and host structure. In other words, the Bernoulli-Euler model considers the actuators as an integral part of the structure. The distribution of the strains

across the composite structure is illustrated in Figure 2.5.

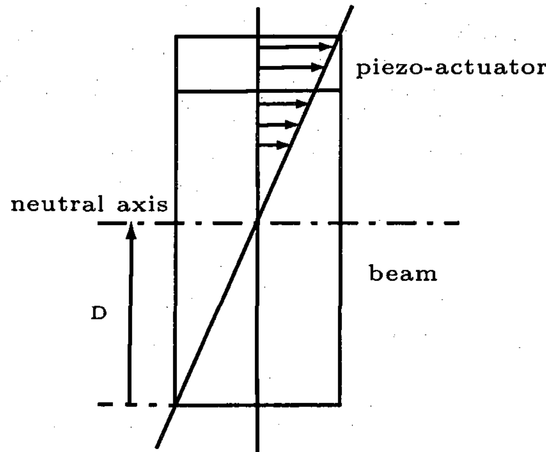

Figure 2.5: Strain distribution in the Bernoulli-Euler model

Three main mechanical models of the distribution of strain within the host cantilever beam and the active piezoelectric actuator have been described above. Two of them have limitations when they are applied to the dynamic analysis of a micro-scale beam structure. The simple blocked force model is unable to correctly predict the actuator/substrate response for thin structure [8]. Usually, the simple blocked force model is applied to analyze macro-scale beam structures, in which the thicknesses of piezoelectric actuators are negligible comparing with the thickness of the macro-scale beam. This approximation just satisfies the assumption of line force source of the actuator in the simple blocked force model.

For the extension case, both uniform strain model and Bernoulli-Euler model can give an accurate prediction [11]. However, the Bernoulli-Euler model is more accurate than the uniform strain model for analyzing bending. The key factor affecting the performance of these two models is the thickness ratio between host structure and piezoelectric materials. At a high thickness ratio, for example more than 5, the two models produce the same results as a finite element model. But for the thickness ratio less than 5, which is the case for a smart micro cantilever beams, the uniform strain model overestimate the strain [11].

Although the first two models have certain limitations on analyzing a micro-scale cantilever beam, the Bernoulli-Euler model, which was proposed by Crawley and Anderson [11], is a feasible model. The validity of this model has already been verified in the analysis of smart micro cantilever beams [53, 54]. Thus, the Bernoulli-Euler model is also adopted here. In order to maintain completeness of this work, the important procedures and results of the Bernoulli-Euler model are presented based on the configuration of the proposed smart cantilever beam, shown in Figure 2.5.

Based on equation (2.2), the moment produced by attaching the piezoelectric actuator is expressed

$$M = \int_{h_c-D}^{h_c+h_p-D} E_p \varepsilon_p w y dy \tag{2.3}$$

where E_p is the Young's modulus of the piezoelectric actuator. If the total thickness of the composite structure is thin compared the radius of curvature, a linear strain distribution may be assumed across the thickness direction and this would also be true for the corresponding stress distribution [24]. Thus, according to the force balance on the neutral axis in the longitudinal direction, the position of the neutral axis D is calculated.

$$E_p w \int_{h_c-D}^{h_c+h_p-D} y dy + E_c w \int_{-D}^{h_c-D} y dy = 0, \tag{2.4}$$

$$D = \frac{E_c h_c^2 + E_p h_p^2 + 2E_p h_p h_c}{2(E_c h_c + E_p h_p)}. \tag{2.5}$$

The Young's modulus of the cantilever beam is represented by E_c. Substituting equation (2.5) into equation (2.3), a relationship between the induced moment M and the input voltage of the piezoelectric actuator $V(t)$ is obtained in equation (2.6).

$$M = C_0 V(t), \tag{2.6}$$

where

$$C_0 = \frac{w E_p E_c h_c (h_c + h_p)}{2(E_c h_c + E_p h_p)} d_{31}. \tag{2.7}$$

The transverse electric charge constant of the piezoelectric materials is represented by d_{31}. Note that for the configuration shown in Figure 2.1, the piezoelectric actuator produces an

axial force as well as a bending moment. However, this axial force is negligible for small transverse vibrations of the smart micro cantilever beam.

2.3 Dynamic Model of the Smart Micro Cantilever Beam

After the equivalent bending moment is selected, the nonuniformity of the cantilever beam is considered for developing the dynamic model. The piece-wise varying configurations are considered as two stepped variations on both geometry and materials due to comparable thickness of the beam and the bonded actuator. This partitioning along with the profile of the induced bending moment is shown in Figure 2.6. For a similar beam with one stepped change on geometry, a two-segmented continuous Euler-Bernoulli beam model was developed to analytically discuss its dynamics [23]. Thus, a three-segmented continuous Euler-Bernoulli beam model is combined with the induced moment and the base excitation to develop the dynamic model of the smart micro cantilever beam.

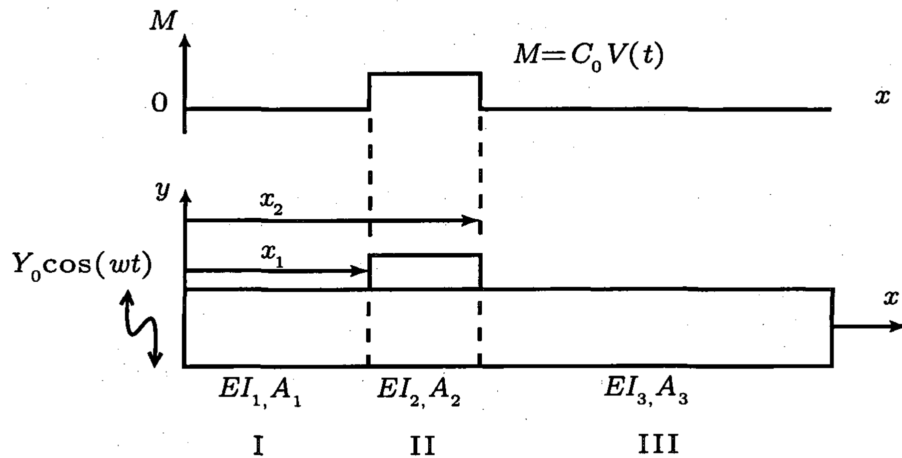

Figure 2.6: The configuration of the smart micro cantilever beam with two stepped variations on the geometry, materials and induced moment.

Generally, the governing equation of an ordinary Euler-Bernoulli beam is shown:

$$\frac{\partial^2}{\partial x^2}\left(EI\frac{\partial^2 \tilde{y}(x,t)}{\partial x^2}\right) + \rho A\frac{\partial^2 \tilde{y}(x,t)}{\partial t^2} = 0 \tag{2.8}$$

where E is the Young's module, I is the moment inertia, ρ is the density of the beam and A is the cross-sectional area.

When a base excitation is introduced, as shown in Figure 2.6, the vertical displacement $\tilde{y}(x,t)$ is modified by a moving reference frame [33] as

$$\tilde{y}(x,t) = y(x,t) + Y_0 \cos(\omega t), \tag{2.9}$$

where Y_0 is the amplitude of the base excitation and ω is the driving frequency. The additional input from the piezoelectric actuator introduces the moment M from equation (2.6) into the three-segmented Euler-Bernoulli governing equation and corresponding boundary conditions, shown in equation (2.10) and equation (2.11).

$$EI_m\frac{\partial^4 y_m(x,t)}{\partial x^4} + \rho A_m\frac{\partial^2 y_m(x,t)}{\partial t^2} = \rho A_m Y_0 \omega^2 \cos(\omega t). \tag{2.10}$$

$$\begin{aligned}
x = 0 \quad &: \quad y_1(0,t) = 0,\\
&\quad\;\; y_1'(0,t) = 0,\\
x = x_1 \quad &: \quad y_1(x_1,t) = y_2(x_1,t),\\
&\quad\;\; y_1'(x_1,t) = y_2'(x_1,t),\\
&\quad\;\; EI_1 y_1''(x_1,t) = EI_2 y_2''(x_1,t) + M,\\
&\quad\;\; EI_1 y_1'''(x_1,t) = EI_2 y_2'''(x_1,t),\\
x = x_2 \quad &: \quad y_2(x_2,t) = y_3(x_2,t),\\
&\quad\;\; y_2'(x_2,t) = y_3'(x_2,t),\\
&\quad\;\; EI_2 y_2''(x_2,t) = EI_3 y_3''(x_2,t) - M,\\
&\quad\;\; EI_2 y_2'''(x_2,t) = EI_3 y_3'''(x_2,t),\\
x = L \quad &: \quad EI_3 y_3''(L,t) = 0,\\
&\quad\;\; EI_3 y_3'''(L,t) = 0.
\end{aligned} \tag{2.11}$$

where

$$EI_1 = EI_3 = E_c I_c \tag{2.12}$$

$$\begin{aligned} EI_2 &= E_c I_c + w E_c h_c \left(\frac{h_c}{2} - D\right)^2 \\ &\quad + E_p I_p + w E_p h_p \left(\frac{h_p}{2} + h_c - D\right)^2 \end{aligned} \tag{2.13}$$

The subscript m is used to identify the three different sections of the smart micro cantilever beam as shown in Figure 2.6. Effective bending stiffness and mass per unit length of different sections are represented by EI_m and ρA_m, respectively. The initial and terminal position of the piezoelectric actuator are x_1 and x_2, respectively. Furthermore, the governing equation of the second section ($m = 2$) includes a moment term introduced by the piezoelectric actuator. However, since the moment described by the Bernoulli-Euler model is independent of x, the moment term is eliminated by taking the second derivatives with respect to x.

From the three governing equations (2.10) and twelve boundary conditions (2.11), the resulting system consists of nonhomogeneous partial differential equations (PDEs) with nonhomogeneous boundary conditions and the nonhomogeneous terms are functions of time. In order to solve this type of problem, it is equivalently divided into two problems. One is homogeneous PDEs with nonhomogeneous boundary conditions and the other is nonhomogeneous PDEs with homogeneous boundary conditions [51]. The details are shown in the following.

The form of $y_m(x,t)$ is assumed to be that of equation (2.14).

$$y_m(x,t) = \varphi_m(x,t) + w_m(x,t). \tag{2.14}$$

Within this equation, $\varphi_m(x,t)$ is a special solution satisfying the nonhomogeneous boundary conditions and $w_m(x,t)$ satisfies the corresponding homogeneous boundary conditions. Substituting equation (2.14) into equation (2.10) and equation (2.11), the special solution is determined by solving the following homogeneous PDEs with nonhomogeneous boundary conditions.

$$EI_m \frac{\partial^4 \varphi_m(x,t)}{\partial x^4} = 0. \tag{2.15}$$

$$\begin{aligned}
x = 0 \ &: \ \varphi_1(0,t) = 0 \\
&\quad \varphi_1'(0,t) = 0 \\
x = x_1 \ &: \ \varphi_1(x_1,t) = \varphi_2(x_1,t) \\
&\quad \varphi_1'(x_1,t) = \varphi_2'(x_1,t) \\
&\quad EI_1\varphi_1''(x_1,t) = EI_2\varphi_2''(x_1,t) + C_0V(t) \\
&\quad EI_1\varphi_1'''(x_1,t) = EI_2\varphi_2'''(x_1,t) \\
x = x_2 \ &: \ \varphi_2(x_2,t) = \varphi_3(x_2,t) \\
&\quad \varphi_2'(x_2,t) = \varphi_3'(x_2,t) \\
&\quad EI_2\varphi_2''(x_2,t) = EI_3\varphi_3''(x_2,t) - C_0V(t) \\
&\quad EI_2\varphi_2'''(x_2,t) = EI_3\varphi_3'''(x_2,t) \\
x = L \ &: \ EI_3\varphi_3''(L,t) = 0 \\
&\quad EI_3\varphi_3'''(L,t) = 0
\end{aligned} \tag{2.16}$$

This problem is solved by assuming that $\varphi_m(x,t)$ is a fourth order polynomial function of x multiplied by $V(t)$. Based on twelve boundary conditions, the special solution is obtained.

$$\begin{aligned}
\varphi_1(x,t) &= 0, \\
\varphi_2(x,t) &= -\frac{C_0V(t)}{2E_2I_2}(x - x_1)^2, \\
\varphi_3(x,t) &= \frac{C_0V(t)}{2E_2I_2}\left[2(x_1 - x_2)x + x_2^2 - x_1^2\right].
\end{aligned} \tag{2.17}$$

Next, the general solution $w_m(x,t)$ is obtained by solving nonhomogeneous PDEs with homogeneous boundary conditions. Substituting equation (2.14) into equation (2.10), then

equations (2.10) and (2.11) becomes

$$EI_m \frac{\partial^4 w_m(x,t)}{\partial x^4} + \rho A_m \frac{\partial^2 w_m(x,t)}{\partial t^2} = \rho A_m \left[Y_0 \omega^2 \cos(\omega t) - \frac{\partial^2 \varphi_m(x,t)}{\partial t^2} \right] \tag{2.18}$$

with homogeneous boundary conditions

$$\begin{aligned}
x = 0 \ &: \ w_1(0,t) = 0 \\
& \quad w_1'(0,t) = 0 \\
x = x_1 \ &: \ w_1(x_1,t) = w_2(x_1,t) \\
& \quad w_1'(x_1,t) = w_2'(x_1,t) \\
& \quad EI_1 w_1''(x_1,t) = EI_2 w_2''(x_1,t) \\
& \quad EI_1 w_1'''(x_1,t) = EI_2 w_2'''(x_1,t) \\
x = x_2 \ &: \ w_2(x_2,t) = w_3(x_2,t) \\
& \quad w_2'(x_2,t) = w_3'(x_2,t) \\
& \quad EI_2 w_2''(x_2,t) = EI_3 w_3''(x_2,t) \\
& \quad EI_2 w_2'''(x_2,t) = EI_3 w_3'''(x_2,t) \\
x = L \ &: \ EI_3 w_3''(L,t) = 0 \\
& \quad EI_3 w_3'''(L,t) = 0
\end{aligned} \tag{2.19}$$

From the method of eigenfunction expansion, the general solution is assumed to have a form of equation (2.20).

$$w_m(x,t) = \sum_{n=1}^{\infty} \phi_{mn}(x) q_n(t) . \tag{2.20}$$

Within the summation, $\phi_{mn}(x)$ is the mth section of the nth mode shape of the piece-wise cantilever beam represented by

$$\phi_{mn}(x) = C_{m1} sin(k_{mn}x) + C_{m2} cos(k_{mn}x) + C_{m3} sinh(k_{mn}x) + C_{m4} cosh(k_{mn}x), \tag{2.21}$$

and $q_n(t)$ is the generalized modal coordinate. The twelve coefficients $C_{mr}, r = 1,2,3,4$ in the mode shapes can be obtained from the eigenvalue problem based on homogeneous

boundary conditions. The form of the generalized modal coordinate $q_n(t)$ is determined by solving the decoupled resonant vibration problem.

The Galerkin method is applied by substituting equation (2.20) into equation (2.18), multiplying the resulting equation by the mode shape $\phi_{mr}(x)$, and integrating across the length of the beam. Due to the orthogonality property of the mode shapes, the following equation is obtained.

$$\ddot{q}_n(t) + 2\zeta_n\omega_n\dot{q}_n(t) + \omega_n^2 q_n(t) = \frac{\left[F_{1n}(Y_0) - F_{2n}(V_0)\right]\omega^2\cos(\omega t)}{I} \tag{2.22}$$

where

$$\begin{aligned}
\omega_n^2 &= \frac{\int_0^L \sum_{m=1}^{3} EI_m\left[\phi''_{mn}(x)\right]^2 dx}{\int_0^L \sum_{m=1}^{3} \rho A_m \phi_{mn}^2(x)dx} \\
I &= \int_0^L \sum_{m=1}^{3} \rho A_m \phi_{mn}^2(x)dx \\
F_{1n}(Y_0) &= Y_0 \int_0^L \sum_{m=1}^{3} \rho A_m \phi_{mn}(x)dx \\
F_{2n}(V_0) &= V_0 \int_0^L \sum_{m=1}^{3} \rho A_m \frac{\varphi_m(x,t)}{V(t)} \phi_{mn}(x)dx
\end{aligned} \tag{2.23}$$

and ζ_n is the nth proportional damping ratio. The eigenfrequency of the smart cantilever beam is represented by ω_n and I is the generalized mass. V_0 represents the magnitude of the input voltage by setting $V(t) = V_0\cos(\omega t)$ for resonant response. The general forces, $F_{1n}(Y_0)$ and $F_{2n}(V_0)$, result from the base excitation and the piezoelectric actuator, respectively. Thus, a steady state resonant responses $(\omega = \omega_n)$ is obtained from equation (2.22)

$$q_n(t) = \frac{\left[F_{1n}(Y_0) + F_{2n}(V_0)\right]\cos\left(\omega_n t - \frac{\pi}{2}\right)}{2I\zeta_n}. \tag{2.24}$$

Finally, the solution for the system given by equation (2.10) and equation (2.11) is

obtained

$$y(x,t) = \begin{cases} \varphi_1(x,t) + w_1(x,t), 0 < x < x_1, \\ \varphi_2(x,t) + w_2(x,t), x_1 \leq x \leq x_2, \\ \varphi_3(x,t) + w_3(x,t), x_2 < x < L. \end{cases} \quad (2.25)$$

The definition of $\varphi_m(x,t)$ is shown in equation (2.17) and $w_m(x,t)$ is obtained from equations (2.20), (2.21) and (2.24).

2.4 Discussion

In the literature, a variety of models and solving methods have been explored for various configurations of smart micro cantilever beams. Zhang et al. [54] studied a tipless cantilever beam with one bonded piezoelectric patch, which is similar to the configuration shown in Figure 2.1. After representing the piezoelectric patch as an external moment, the Euler-Bernoulli beam model was used to approximately describe the nonuniform beam structure and solved by the Rayleigh-Ritz method. Due to this approximation, the obtained solution consists of modal solutions without the special solution part shown in equation (2.25).

Furthermore, an adaptable end effector, represented by attaching one piezoceramic layer on a portion of an AFM probe, was modeled as a two-segmented Euler-Bernoulli beam with an induced moment applied at the interior boundary from the layer [53]. The modal solution of this model was obtained by solving an alternative Lagrange equation with the assumed mode-summation method. Recently, Salehi-Khojin et al. [43] developed a three-section Euler-Bernoulli beam model excited by a moment from the piezoelectric actuator for an active AFM probe, which had two discontinuities along the probe: one was due to the end of the piezoelectric layer and the other was due to the sudden decrease on the cross-section. The expansion theorem [51] and the method of assumed modes [32] were used to solve this model. In the two cases above, although the segmented Euler-Bernoulli beam model is used according to various step changes in geometry or materials,

the obtained solutions are all based on modal solutions. We will show in the next chapter how the special solution $\varphi_m(x,t)$ shown in equation (2.25) contributes to the adjustable tip trajectories.

Chapter 3

Tip Trajectory Characterization

Motivated from Chapter 1, tip trajectories are key to nanomanipulation since the tip directly interacts with nano-scale objects. In this chapter, the equation describing the tip trajectory is derived from the motion of the free end of the AFM probe based on its geometric relationship with the probe tip. One typical tip trajectory is plotted and characterized according to the description equation.

3.1 Tip Trajectory Derivation

From equation (2.25), the vibration of the smart micro cantilever beam consists of two parts. The first part $\varphi_m(x,t)$ is the special solution which consists of a second order polynomial of x while the second part $w_m(x,t)$ is the modal solution which consists of a summation of infinite eigenmodes along x. When two excitations are applied at one single eigenfrequency, the corresponding eigenmode approximately represents the modal solution. Thus, the resonant vibration of the smart micro cantilever beam is regarded as one combination of a second order polynomial and the modal solution at one single eigenmode.

As shown in Figure 3.1, the modal solution at the second eigenmode has a strong interaction with the special solution since their amplitudes are comparable given a reasonable input pair in AFM systems. Furthermore, the amplitudes of the two parts of the solution are related to the inputs, V_0 and Y_0. Thus, by adjusting the two inputs, a suitable combination of the two portions of the solution contribute to a desirable trajectory. In this manner, excitations at the second eigenfrequency of the smart cantilever beam generate

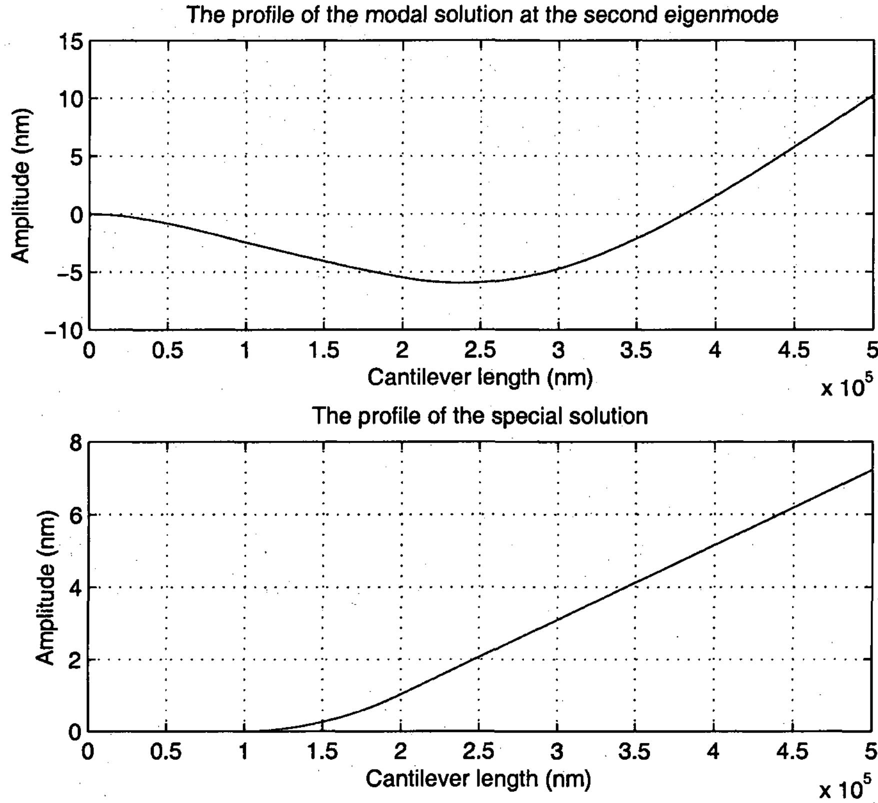

Figure 3.1: The profile of the modal solution at the second eigenmode and the profile of the special solution when $Y_0 = 2$ nm and $V_0 = 1$ volt.

an elliptical tip trajectory.

As shown in Figure 3.2, the tip is assumed to be located at the free end of the cantilever beam. The length of the tip is represented by h and the slope at the end of the cantilever beam is defined in equation (3.1).

$$K\left(L,t\right) = y'(x,t)|_{x=L}. \tag{3.1}$$

The relationship between the dynamic position of the free end of the cantilever beam and the end of the tip is obtained as follows.

$$y_{tip}\left(t\right) - y\left(L,t\right) = -\frac{1}{K\left(L,t\right)}\left(x_{tip}\left(t\right) - L\right) \tag{3.2}$$

$$\left[y_{tip}\left(t\right) - y\left(L,t\right)\right]^2 + \left[x_{tip}\left(t\right) - L\right]^2 = h^2 \tag{3.3}$$

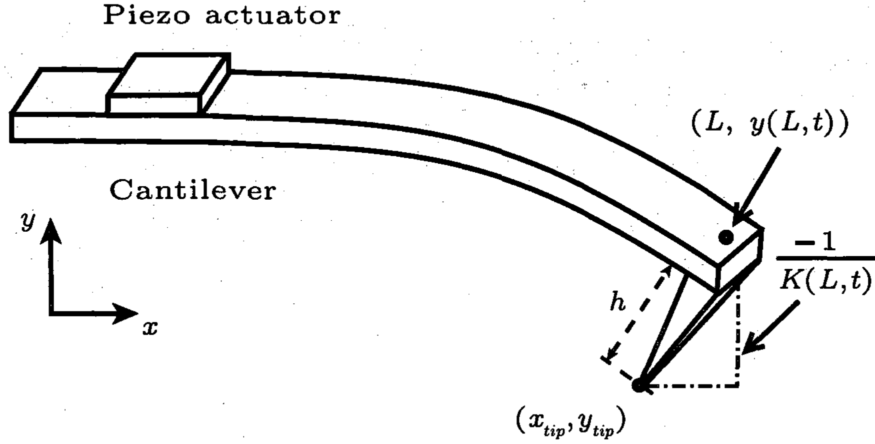

Figure 3.2: The geometry relationship between the free end of the smart micro cantilever beam and the end of the tip.

The coordinate of the end of the tip is identified as $(x_{tip}(t)\,,\ y_{tip}(t))$. The perpendicular relationship between the slope $K(L,t)$ and the tip leads to equation (3.2) and equation (3.3) is obtained by using the Pythagorean theorem. Note that the abscissa of the free end is remained at L because the deflection of the beam is very small compared to the length of the beam. By solving equation (3.2) and equation (3.3) for the coordinate at the end of the tip, $x_{tip}(t)$ and $y_{tip}(t)$ are obtained.

$$x_{tip}(t) = L + \frac{K(L,t)\,h}{\sqrt{K(L,t)^2+1}}, \tag{3.4}$$

$$y_{tip}(t) = y(L,t) - \frac{h}{\sqrt{K(L,t)^2+1}}. \tag{3.5}$$

Since $K(L,t)$ is much smaller than 1 when a micro-scale cantilever beam vibrates with nano-scale amplitudes, equation (3.4) and equation (3.5) are simplified as

$$\frac{x_{tip}-L}{h} = K(L,t) \tag{3.6}$$

$$y_{tip}+h = y(L,t) \tag{3.7}$$

Based on equation (2.25), the solution and the slope at the free end of the smart micro

cantilever beam are written as

$$y(L,t) = \left[\phi_{3n}(x)\, q_n(t) + \varphi_3(x,t)\right]|_{x=L} = \left(f_1 Y_0 + f_2 V_0\right)\sin(\omega_n t) + f_3 V_0 \cos(\omega_n t) \tag{3.8}$$

$$K(L,t) = \left[\phi'_{3n}(x)\, q_n(t) + \varphi'_3(x,t)\right]|_{x=L} = \left(\hat{f}_1 Y_0 + \hat{f}_2 V_0\right)\sin(\omega_n t) + \hat{f}_3 V_0 \cos(\omega_n t) \tag{3.9}$$

where

$$\begin{aligned} f_1 &= \frac{\phi_{3n}(L)\, F_{1n}(Y_0)}{2I\zeta_n Y_0} \\ f_2 &= \frac{\phi_{3n}(L)\, F_{2n}(V_0)}{2I\zeta_n V_0} \\ f_3 &= \varphi_3(L) \\ \hat{f}_1 &= \frac{\phi'_{3n}(L)\, F_{1n}(Y_0)}{2I\zeta_n Y_0} \\ \hat{f}_2 &= \frac{\phi'_{3n}(L)\, F_{2n}(V_0)}{2I\zeta_n V_0} \\ \hat{f}_3 &= \varphi'_3(L) \end{aligned} \tag{3.10}$$

Combining equations (3.8), (3.9), (3.6) and (3.7), the ellipse equation of the trajectory (3.11) is obtained by canceling the time parameter t with trigonometric identities.

$$\frac{(x_{tip} - L)^2}{\hat{a}^2} + \frac{(y_{tip} + h)^2}{\hat{b}^2} + 2c\,(x_{tip} - L)\,(y_{tip} + h) = V_0^2 e \tag{3.11}$$

where

$$
\begin{aligned}
\alpha &= \frac{Y_0}{V_0} \\
\hat{a}^2 &= V_0^2 h^2 \left[\left(\hat{f}_1 \alpha + \hat{f}_2 \right)^2 + \left(\hat{f}_3 \right)^2 \right] \\
\hat{b}^2 &= V_0^2 \left[(f_1 \alpha + f_2)^2 + (f_3)^2 \right] \\
c &= -\frac{f_1 \hat{f}_1 \alpha^2 + \left(f_1 \hat{f}_2 + f_2 \hat{f}_1 \right) \alpha + f_3 \hat{f}_3 + f_2 \hat{f}_2}{h \left[\left(\hat{f}_1 \alpha + \hat{f}_2 \right)^2 + \hat{f}_3^2 \right] \left[(f_1 \alpha + f_2)^2 + f_3^2 \right]} \\
e &= \frac{\left[\left(f_1 \hat{f}_3 - f_3 \hat{f}_1 \right) \alpha + \left(f_2 \hat{f}_3 - f_3 \hat{f}_2 \right) \right]^2}{\left[\left(\hat{f}_1 \alpha + \hat{f}_2 \right)^2 + \hat{f}_3^2 \right] \left[(f_1 \alpha + f_2)^2 + f_3^2 \right]}
\end{aligned}
\tag{3.12}
$$

The input ratio is represented by α. Characteristic parameters of the rotated ellipse are $\hat{a}$, $\hat{b}$, c and e. Generalized forces are represented by f_s, $\hat{f}_s$ for $s = 1, 2, 3$.

3.2 Characterization

Given a pair of suitable inputs from commercial AFM systems, $Y_0 = 2$ nm and $V_0 = 1$ volt, an elliptical trajectory with the rotation angle θ, the semiminor axis a and semimajor axis b is shown in Figure 3.3. This local coordinate figure is plotted according to the trajectory equation (3.11) while the center of the ellipse located at $(L, -h)$ is moved to the origin. The rotation angle θ between the vertical axis and the semimajor axis in the clockwise direction shown in Figure 3.3 is defined in equation (3.13).

$$
\theta = \frac{1}{2} \arctan \left(\frac{c_1 \alpha^2 + c_2 \alpha + c_3}{d_1 \alpha^2 + d_2 \alpha + d_3} \right) \tag{3.13}
$$

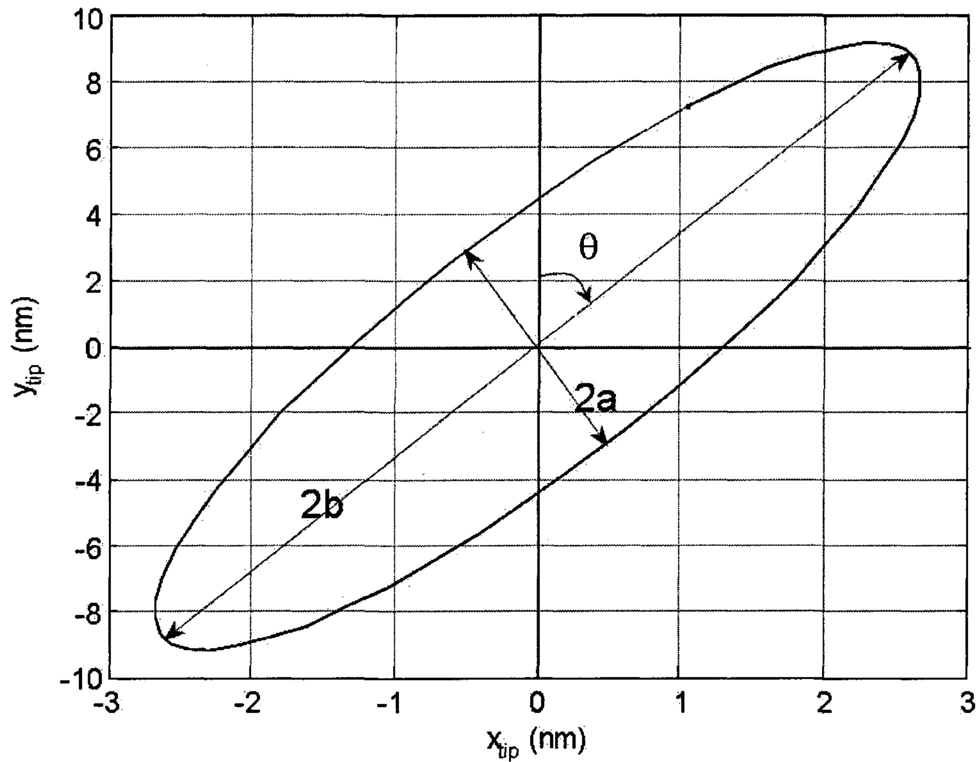

Figure 3.3: An elliptical trajectory of the end of the tip with the semiminor axis a, the semimajor axis b and the rotation angle θ.

The parameters c_s and d_s for $s = 1, 2, 3$ are shown in equation (3.14).

$$
\begin{aligned}
c_1 &= -2hf_1\hat{f}_1 \\
c_2 &= -2h\left(f_1\hat{f}_2 + f_2\hat{f}_1\right) \\
c_3 &= -2h\left(f_3\hat{f}_3 + f_2\hat{f}_2\right) \\
d_1 &= f_1^2 - h^2\hat{f}_1^2 \\
d_2 &= 2f_1f_2 - 2h^2\hat{f}_1\hat{f}_2 \\
d_3 &= f_2^2 + f_3^2 - h^2\left(\hat{f}_2^2 + \hat{f}_3^2\right)
\end{aligned}
\tag{3.14}
$$

Since these coefficients are independent of the inputs, the rotation angle is a function of the input ratio. Thus, as long as the input ratio does not change, the rotation angle will

remain the same with different inputs.

The semiminor axis a and semimajor axis b are presented in equation (3.15) and equation (3.16).

$$a = V_0\sqrt{\frac{e\cos(2\theta)}{\frac{1}{\hat{a}^2}\cos^2(\theta) - \frac{1}{\hat{b}^2}\sin^2(\theta)}} \tag{3.15}$$

$$b = V_0\sqrt{\frac{-e\cos(2\theta)}{\frac{1}{\hat{a}^2}\sin^2(\theta) - \frac{1}{\hat{b}^2}\cos^2(\theta)}} \tag{3.16}$$

Since $\hat{a}$ and $\hat{b}$ are functions of V_0^2 in equation (3.12), a and b are proportional to V_0^2 when the input ratio remains the same. All the characteristic parameters of the elliptical trajectory, θ, a and b, are discussed in detail in next chapter.

Chapter 4

Simulation Results and Discussion

4.1 Elliptical and Linear Tip Trajectory

Based on the ellipse equation (3.11) and the related parameters defined by equations (3.13), (3.15) and (3.16), the predicted tip trajectories of the smart micro cantilever beam are examined. The parameter values used for the simulations are given in Table 4.1. Most of these parameters are taken from the work of Zhang et al. [53], which were used to describe a commercial AFM probe. Additional parameters such as the location of the piezoelectrical actuator are added for the purpose of this work. In an effort to maintain realistic behavior, the input signals are within suitable ranges of commercial AFM systems.

From equation (3.13), the rotation angle is represented as a function of the input ratio, which is displayed in Figure 4.1. The rotation angle θ varies from 8° to 23° when the tip length is equal to $\frac{L}{10}$. Through the coefficients c_s and d_s, the length of the tip is also determined to influence the rotation angle. By decreasing the tip length, the range of the rotation angle decreases and the values become smaller. For example, the range of the rotation angle is from 4° to 12° for a tip length of $h = \frac{L}{20}$. By increasing the tip length, the range of the rotation angle becomes larger and the values of the rotation angle also increase. The rotation angle has a range from 16° to 41° for a tip length of $h = \frac{L}{5}$. These trends are shown in Figure 4.1.

Although the rotation angle is not influenced by any independent input as long as the input ratio remains the same, the semimajor and semiminor axes are determined by both the input ratio and the value of the input voltage. Figure 4.2 qualitatively shows the trend

Table 4.1: Parameters for simulation.

Parameters	Symbol	Values
Cantilever length	L	500 μm
Piezo length	l_p	100 μm
Piezo and cantilever width	w	250 μm
Piezo thickness	h_p	3.5 μm
Piezo Young's modulus	E_p	120 GPa
Piezo density	ρ_p	5.2 g/cm^3
Cantilever thickness	h_c	4 μm
Cantilever Young's modulus	E_c	169 GPa
Cantilever density	ρ_c	2.33 g/cm^3
Piezo location	x_1	100 μm
Electric charge constant	d_{31}	3.7 pm/V
Tip length	h	0.1L
Damping coefficient	ζ_2	0.007

of the tip trajectories for various input combinations. The horizontal and longitudinal coordinates for each small curve stand for different inputs. For each small curve, it is plotted as that in Figure 3.3. The trend lines clock-wise labeled from A to I are used to characterize specific trends in the trajectories. The special diagonal trend line E is discussed first.

The trend line E corresponds to the case when the rotation angle remains equal to the minimum value. The same rotation angle resulting from the unchanged input ratio agrees with the previous discussion regarding the rotation angle. The semimajor and semiminor axes are both proportional to the input voltage as long as the value of the input ratio remains unchanged, which is described by equation (3.15) and (3.16). The

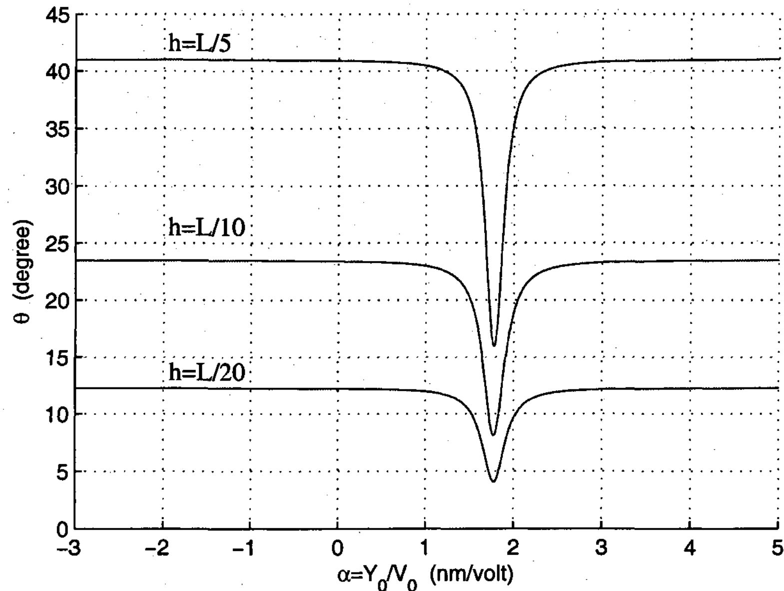

Figure 4.1: The variation of the rotation angle with different input ratios and tip lengths.

trend line E divides the $V_0 - Y_0$ plane into two regions. The upper portion is dominated by base-excitation and the lower portion is dominated by piezo-excitation.

Next, two limiting cases are considered. In these two cases, there is only one excitation source. When only the piezoelectric actuator is excited, the trajectories on the trend line I are elliptical. By increasing the input voltage, the rotation angle remains at the maximum value, the semimajor axis increases greatly and the semiminor axis also increases but less rapidly. When only the base excitation input is applied, the trajectories on the trend line A become linear, which corresponds to an ellipse where the semiminor axis is equal to zero. By increasing the amplitude of the base excitation, the rotation angle remains at the maximum value and the length of linear trajectories increases.

For general cases, the trend lines B, C and D display trends of the trajectories when V_0 remains the same and Y_0 increases. The rotation angles decrease to a minimum value when the curves approach the trend line E and then returns to the maximum value as the value of Y_0 continues to increase. At the same time, the semimajor axes and the semiminor

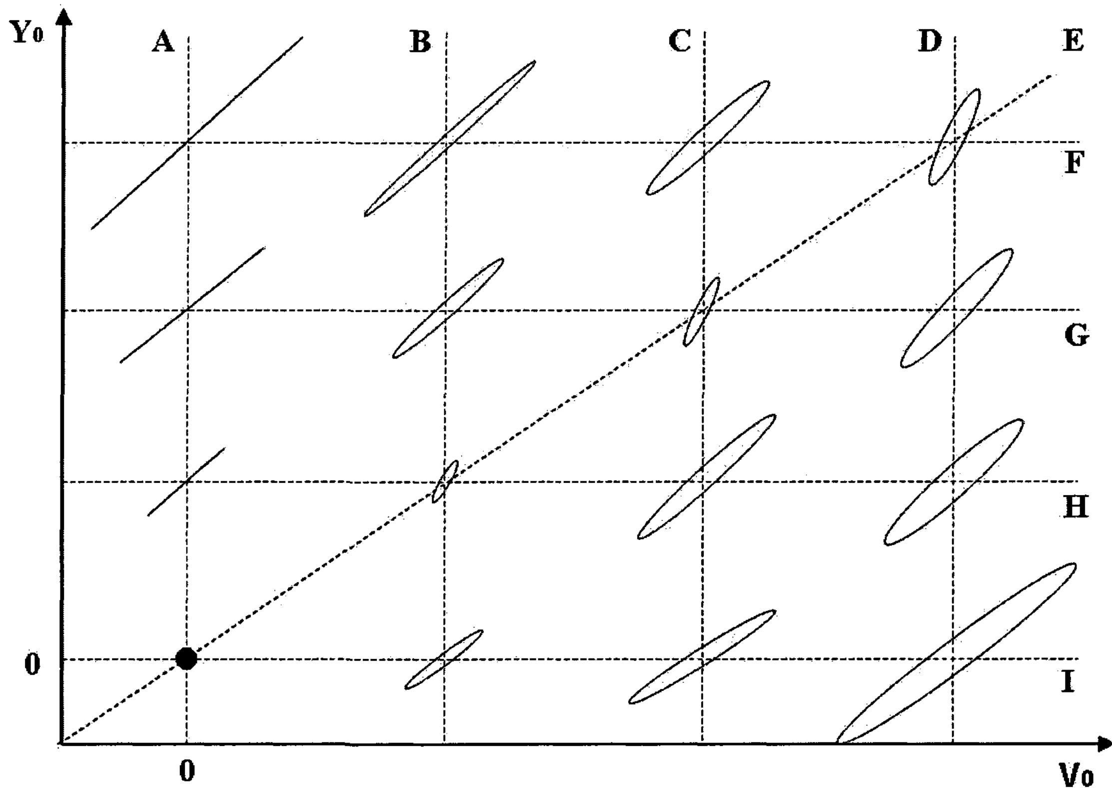

Figure 4.2: The trends of tip trajectories corresponding to different inputs.

axes also decrease towards the trend line E and then increase away from it. Fig. 4.3 quantitatively displays the variation of a and b in this case. Furthermore, the semimajor and semiminor axes achieve minimum values at the same value of Y_0 for a given V_0. This ratio $\frac{Y_0}{V_0}$ is exactly the value which makes the rotation angle θ reach the minimum value shown in Fig. 4.1. The semimajor axis changes linearly and the semiminor axis does not change much except around the minimum value.

The trend lines F, G and H display trends of the tip trajectories when Y_0 remains the same and the value of V_0 increases. The rotation angles and the semimajor axes display similar trends as was observed for the trend lines B, C and D. That is, they first decrease as the increasing input approaches the trend line E and then increase when the input is increased further. However, the semiminor axes with the increase of V_0 are observed to produce a different trend than what was previously observed for trend lines B, C and D.

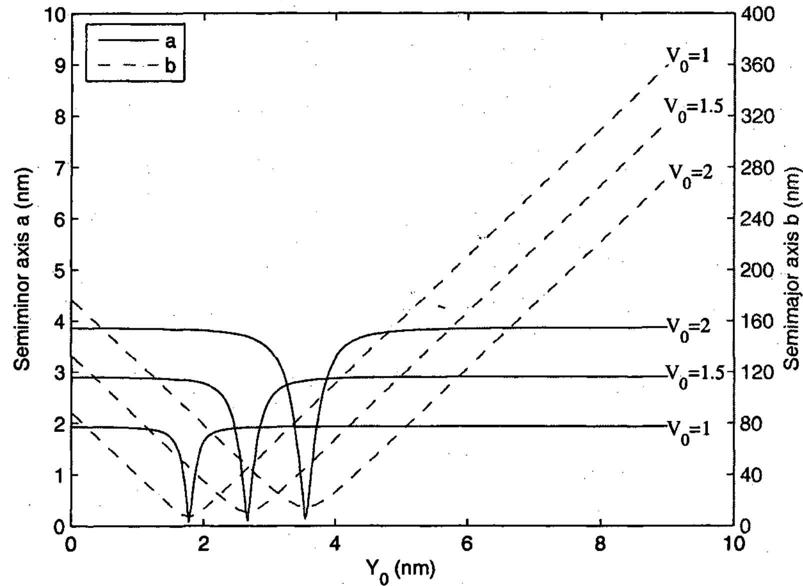

Figure 4.3: The variation of the semiminor axis (solid line) and semimajor axis (dashed line) with continuous increase of Y_0.

They first increase from zeros, then decrease towards the trend line E, and increase again away from it. Fig. 4.4 quantitatively displays the variation of semiminor and semimajor axes of curves on the trend lines F, G and H in Fig. 4.2. Again, a and b achieve minimum values at the same value of V_0 for a given Y_0. The rotation angle θ also reaches the minimum value for this input ratio. The semimajor axis changes linearly except around the minimum value. However, the semiminor axis increases linearly with the exception of a minimum occurring at the voltage corresponding the input ratio represented on the trend line E.

The different trends observed in Fig. 4.3 and Fig. 4.4 for the semiminor axis indicate that the two inputs, Y_0 and V_0, influence the response of the smart micro cantilever beam differently.

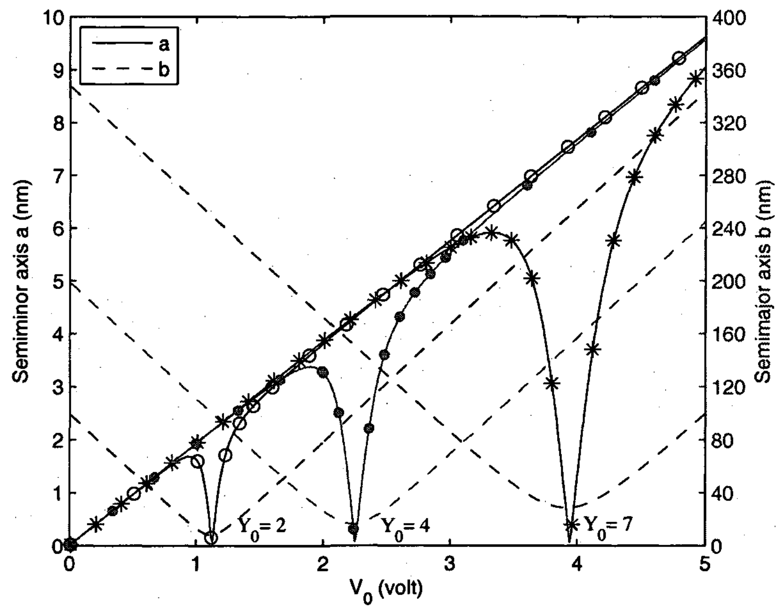

Figure 4.4: The variation of the semiminor axis (solid line) and semimajor axis (dashed line) with continuous increase of V_0.

Table 4.2: The trends of tip trajectories.

Trends	Inputs	θ	a	b
E	$V_0 \uparrow$, $Y_0 \uparrow$, $\Delta \frac{Y_0}{V_0} = 0$	remain the same	increase proportional to V_0	increase proportional to V_0
I	$V_0 \uparrow$, $Y_0 = 0$	remain the same	increase slowly	increase dramatically
A	$Y_0 \uparrow$, $V_0 = 0$	remain the same	$a \equiv 0$	increase dramatically
B, C, D	$Y_0 \uparrow$, $\Delta V_0 = 0$	decrease to minimums on E then increase to maximums	decrease to minimums on E then increase to maximums	decrease to minimums on E then increase extensively
F, G, H	$V_0 \uparrow$, $\Delta Y_0 = 0$	decrease to minimums on E then increase to maximums	increase from zero, decrease to minimums on E then increase	decrease to minimums on E then increase extensively

The trends of the elliptical and linear trajectories are summarized in Table 4.2. The first column lists all the trend lines shown in Figure 4.2. The second column shows how the two independent inputs vary along the corresponding trend lines. The third to fifth columns display how the characteristics of the tip trajectories change along the corresponding trend lines.

4.2 Applications in Nanomanipulation

Based on the characterization of tip trajectories in the previous section, these trajectories are classified into two groups: linear trajectories with various lengths and elliptical trajectories with different rotational angles and curvatures. Different from the horizontal tip trajectory of the CM probe [36], the length of the linear trajectory which can be adjusted within a large nano-meter range, is proportional to the input voltage, see equation (3.16). Furthermore, the elliptical trajectories display new curved movements of the end of the tip in the range of nano-meters. Thus, from the nano-rubbing application of the horizontal tip trajectory, the elliptical trajectories as well as the linear trajectories are expected to have new utilizations on nanomachining. For example, more complex geometry may be machined by the curved tip trajectories.

The nano-rubbing process by using the horizontal tip trajectory of the CM probe was implemented on the surface of UV-cured resin [36]. When the CM probe was vibrated at the second mode, the tip was kept rubbing the resin surface at ultrasonic frequency. The resulting friction heat melted and coagulated the resin to form the bank. Based on this work, Muraoka et al. proposed that, with larger shear forces in the dynamic rubbing, the grooves will be formed by gradually removing material through multiple passes. Iwata et al. [22] verified this nanomachining process with another similar ultrasonic scratching process. For a static AFM probe in contact with the sample surface, the tip was used to scratch the surface by horizontally oscillating the sample with a quartz crystal resonator. Two materials, polycarbonate films and collagen fibrils, were scratched at

ultrasonic frequency to form grooves. Either by moving the tip or by moving the sample, the horizontal scratching can be used as a nanomachining process for gradually removing materials with an AFM tip.

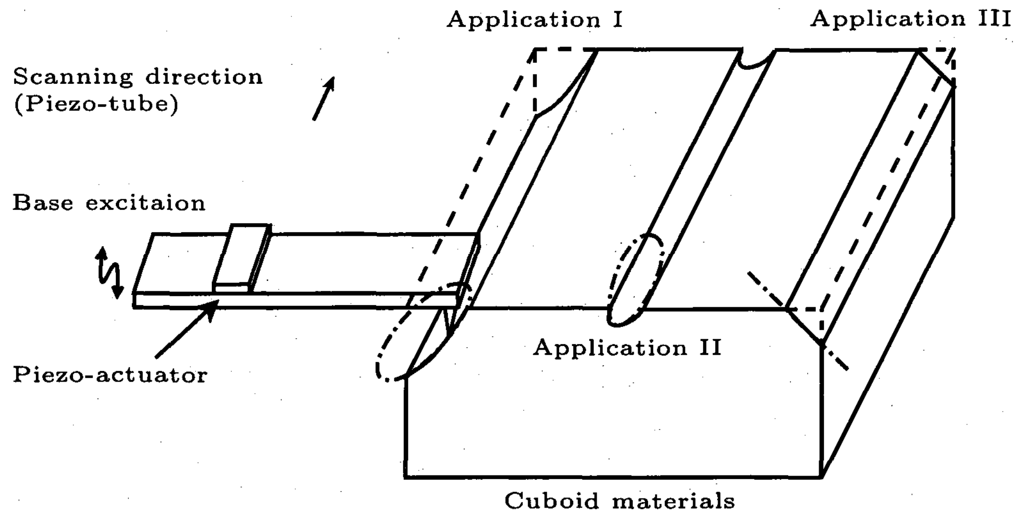

Figure 4.5: Potential applications of resulting trajectories on three-dimensional nanomanipulation. In application I and II, the side portion and bottom portion of an elliptical trajectory can be used to machine a curved plane and a nano-trench, respectively. While a linear trajectory can be applied to shape an inclined plane in application III.

Based on the successful experiments described above, the elliptical and linear trajectories are anticipated to have important applications in nanomanipulation as well. The corresponding three potential applications are proposed for machining a nano-cuboid, shown in Figure 4.5. The first application consists of polishing one edge of the nano-cuboid with an elliptical trajectory. Through a same process as in nano-rubbing [36] and nano-scratching [22], a nano-scale curve is formed at one end of the edge by gradually removing the materials with a controllable and repeatable motion of the tip. Along the scanning direction of the piezo-tube in AFM, a three-dimensional curved nano-plane is able to be shaped. An elliptical trajectory is also used to machine nano-trenches on the surface of the cuboid, which have important applications such as modifying surface diffusion of ultrathin liquid

films [31]. As illustrated in Figure 4.5, the bottom portion of the elliptical trajectory is adopted in the second application. The geometry of the resulting trench depends on the characteristic parameters (a, b and θ) of the elliptical trajectory. The third application is using the linear trajectory, which is a special case of the elliptical trajectory where the semiminor axis a is zero. In this case, an inclined plane is shaped along the scanning direction as shown in Figure 4.5. Note that corresponding to the shape of the inclined plane, the smart micro cantilever beam would be located on the right side of the cuboid.

Furthermore, since the elliptical trajectory is controlled by two inputs Y_0 and V_0, the curvature of the trajectory and consequently the profile of the curved nano-plane can be adjusted *in situ* by tuning the values of the inputs. This property is also true for machining the nano-trench and the inclined plane. Thus, more complex geometry could be shaped by varying the inputs during the machining process. For example, a nano-trench with narrow cross-sectional area at the beginning and gradually larger cross-sectional area along the scanning direction can be machined.

4.3 Discussion

In order to successfully implement these nanomanipulation designs, the resistive forces during machining and the corresponding control laws to compensate for them need to be considered. Since a curved trajectory may encounter a time-varying resistive force during the implementation, average resistive forces modeled as linear damping forces [36, 44] may be calculated from the dissipation energy, which can be measured in many commercial AFM systems. Thus, after the properties of the resistive forces are understood well, the corresponding control laws to compensate for the forces will be designed in order to maintain desired trajectories so that they may be implemented in a real AFM system to study the proposed nanomanipulation.

Chapter 5

Conclusions

Nanomanipulation as an important area of nanotechnology is introduced. A general definition of nanomanipulation is proposed to understand the scope of research in the area of nanomanipulation. Different approaches and tools for nanomanipulation are summarized and discussed. The importance of AFM-based nanomanipulation systems for performing mechanical manipulation processes is emphasized.

Within such an AFM-based system, a smart micro cantilever beam, consisting of an AFM probe bonded with a segment of piezoelectric material, is proposed to produce a variety of nano-scale tip trajectories with potential applications in nanomanipulation. The tip trajectory is derived from the motion of the free end of the cantilever beam based on its geometric relationship with the probe tip. From the resonant responses of the smart micro cantilever beam, elliptical and linear tip trajectories are produced when the second dynamic mode is excited. The lengths of the linear trajectories can be changed within a large nano-meter range *in situ* by adjusting the magnitude of the base excitation. Furthermore, through varying the magnitudes of the base excitation and the piezoelectric actuator independently, the semiminor axis a, the semimajor axis b and the rotational angle θ of the elliptical trajectories may also be adjusted *in situ*. Potential applications of the resulting trajectories for three-dimensional nanomanipulation are proposed.

Bibliography

[1] http://www.nanotech-now.com/nanotechnology-glossary-M-O.htm, April, 2009.

[2] J. D. Adams, B. Rogers, L. Manning, Z. Hu, T. Thundat, H. Cavazos, and S. C. Minne. Piezoelectric Self-sensing of Adsorption-induced Microcantilever Bending. *Sensors and Actuators A*, 121:457–461, 2005.

[3] B. N. Agrawal and K. E. Treanor. Shape Control of A Beam Using Piezoelectric Actuators. *Smart Materials and Structures*, 8:729–739, March 1999.

[4] T. Bailey and J. E. Hubbard. Distributed Piezoelectric-Polymer Active Vibration Control of A Cantilever Beam. *Journal of Guidance, Control and Dynamics*, 8(5):605–611, September 1985.

[5] R. S. Becker, J. A. Golobchenko, and B. S. Swartzentruber. Atomic-scale Surface Modifications using a Tunnelling Microscope. *Nature*, 325:419–421, January 1987.

[6] G. Binnig, C. F. Quate, and Ch. Gerber. Atomic Force Microscope. *Physical Review Letters*, 56(9):930–933, 1986.

[7] F. Biscarini, J. Chen, R. Komanduri, C. Taliani, and C. Doumanidis. Summary Report on Nanomanufacturing and Processing. Technical report, 2002.

[8] Z. Chaudhry and C. A. Rogers. The Pin-Force Model Revisited. *Journal of Intelligent Material Systems and Structures*, 5:347–354, 1994.

[9] I. Chopra. Status of Application of Smart Structures Technology to Rotorcraft Systems. *Journal of the American Helicopter Society*, 45(4):228–252, 2000.

[10] I. Chopra. Review of State of Art of Smart Structures and Integrated Systems. *AIAA Journal*, 40(11):2145–2187, November 2002.

[11] E. F. Crawley and E. H. Anderson. Detailed Models of Piezoceramic Actuation of Beams. *Journal of Intelligent Material Systems and Structures*, 1(1):4–25, January 1990.

[12] J. Cumings and A. Zettl. Low-Friction Nanoscale Linear Bearing Realized from Multiwall Carbon Nanotubes. *Science*, 289:602–604, 2000.

[13] S. Decossas, F. Mazen, T. Baron, G. Brémond, and A. Souifi. Atomic Force Microscopy Nanomanipulation of Silicon Nanocrystals for Nandevice Fabrication. *Nanotechnology*, 14(12):1272–1278, 2003.

[14] C. Doumanidis. Nano-manufacturing: Technical Advances, Research Challenges and Future Directions. Technical report, University of Cyprus, 2005.

[15] E. Du, H. Cui, and Z. Zhu. Review of Nanomanipulators for Nanomanufacturing. *International Journal of Nanomanufacturing*, 1(1):83–104, 2006.

[16] D. M. Eigler and E. K. Schweitzer. Positioning Single Atoms with a Scanning Tunnelling Microscope. *Nature*, pages 524–526, April 1990.

[17] J. S. Foster, J. E. Fforommer, and P. C. Arnett. Molecular Manipulation using a Tunneling Microscope. *Nature*, pages 324–326, January 1988.

[18] K. Fukushima, S. Kawai, D. Saya, and H. Kawakatsu. Measurement of Mechanical Properties of Three-dimensional Nanometric Objects by An Atomic Force Microscope Incorporated in A Scanning Electron Microscope. *Review of Scientific Instruments*, 73(7):2647–2650, 2002.

[19] N. Gurjar and N. Jalili. Toward Ultrasmall Mass Detection Using Adaptive Self-Sensing Piezoelectrically Driven Microcantilevers. *IEEE/ASME Transactions on Mechatronics*, 12(6):680–688, December 2007.

[20] M. Guthold, M. R. Falvo, W. G. Matthews, S. Paulson, S. Washburn, D. A. Erie, R. Superfine, F. P. Brooks, and R. M. Taylor. Controlled Manipulation of Molecular Samples with the Nanomanipulator. *IEEE/ASME Transactions on Mechatronics*, 5(2):189–198, June 2000.

[21] L. T. Hansen and A. Kuhle. A Technique for Positioning Nanoparticles using an Atomic Force Microscope. *Nanotechnology*, 9(4):337–343, 1998.

[22] F. Iwata, K. Ohara, Y. Ishizu, A. Sasaki, H. Aoyama, and T. Ushiki. Nanometer-Scale Manipulation and Ultrasonic Cutting Using An Atomic Force Microscope Controlled by A Haptic Device as A Human Interface. *Japanese Journal of Applied Physics*, 47(7):6181–6185, 2008.

[23] S. K. Jang and C. W. Bert. Free Vibration of Stepped Beams: Exact and Numerical Solutions. *Journal of Sound and Vibration*, 130(2):342–346, 1989.

[24] R. M. Jones. *Mechanics of Composite Materials.* Hemisphere Publishing Company, New York, 1975.

[25] T. Junno, K. Deppert, L. Montelius, and L. Samuelson. Controlled Manipulation of Nanoparticles with an Atomic Force Microscopy. *Applied Physics Letters*, 66(26):3627–3629, June 1995.

[26] M. R. Kermani, R. V. Patel, and M. Moallem. Flexure Control Using Piezostack Actuators: Design and Implementation. *IEEE/ASME Transactions on Mechatronics*, 10(2):181–188, 2005.

[27] T. Kizuka, K. Yamada, S. Deguchi, M. Naruse, and N. Tanaka. Cross-Sectional Time-Resolved High-Resolution Transmission Electron Microscopy of Atomic-Scale Contact and Noncontact-type Scanning on Gold Surfaces. *Physics Review B*, 55:7398–7401, 1997.

[28] B. Klehn and U. Kunze. Nanolithography with An Atomic Force Microscope by means of Vector-scan Controlled Dynamic Plowing. *Journal of Applied Physics*, 85(7):3897–3903, April 1999.

[29] C. Y. Lin, E. F. Crawley, and J. Heeg. Open- and Closed-Loop Results of A Strain-Actuated Active Aeroelastic Wing. *Journal of Aircraft*, 33(5):987–994, 1996.

[30] S. R. Manalis, S. C. Minne, and C. F. Quate. Aomic Force Microscopy for High Speed Imaging Using Cantilevers with An Integrated Actuator and Sensor. *Applied Physics Letters*, 68(6):871–873, February 1996.

[31] M. S. Mayeed, A. M. Al-Mekhnaqi, G. M. Newaz, and T. Kato. Effect of Nano-Trenches on The Ultrathin Liquid Polymer Film Spreading and Free Surface Undulations on Solid Surfaces. *Journal of Nanoengineering and Naonosystems*, 220:157–162, 2006.

[32] L. Meirovitch. *Analytical Methods in Vibrations.* The Macmillan Company, 1967.

[33] L. Meirovitch. *Fundamentals of Vibrations.* Thomas Casson, 2001.

[34] Y. Mualim, F. H. Ghorbel, and J. B. Dabney. Nanomanipulaion Modeling and Simulation. In *Proceedings of ASME'06*, Chicago, November 2006.

[35] M. Muraoka. Vibrational Dynamics of Concentrated-mass Cantilevers in Atomic Force Acoustic Microscopy: Presence of Modes with Selective Enhancement of Vertical or Lateral Tip Motion. *Journal of Physics: Conference Series*, 61:836–840, 2007.

[36] M. Muraoka and H. Ishikawa. Nano Machining by Rubbing at Ultrasonic Frequency Under Controlled Shear Force. Technical report, Akita University, Japan, 2006.

[37] O. Rabinovitch and J. R. Vinson. Adhesive Layer Effects in Surface-mounted Pizoelectric Actuators. *Journal of Intelligent Material Systems and Structures*, 13:689–704, November 2002.

[38] T. R. Ramachandran, C. Baur, A. Bugacov, A. Madhukar, B. E. Koel, A. Requicha, and C. Gazen. Direct and Controlled Manipulation of Nanometer-sized Particles using the Non-contact Atomic Force Microscope. *Nanotechnology*, 9(3):237–245, 1998.

[39] A. Raman, J. Melcher, and R. Tung. Cantilever Dynamics in Atomic Force Microscopy. *Nanotoday*, 3(1–2):20–27, 2008.

[40] R. Resch, A. Bugacov, C. Baur, B. E. Koel, A. Madhukar, A. A. G. Requicha, and P. Will. Manipulation of Nano Particles Using Dynamic Force Microscopy: Simulation and Experiments. *Applied Physics A*, 67:265–271, September 1998.

[41] K. El Rifai, O. El Rifai, and K. Youcef-Toumi. Modeling and Control of AFM-based Nano-manipulation Systems. In *Proceedings of the IEEE International Conference on Robotics and Automation*, pages 157–162, 2005.

[42] F. J. Rubio-Sierra, W. M. Heckl, and R. W. Stark. Nanomanipulation by Atomic Force Microscopy. *Advanced Engineering Materials*, 7(4):193–196, 2005.

[43] A. Salehi-Khojin, S. Bashash, and N. Jalili. Modeling and Experimental Vibration Analysis of Nanomechanical Cantilever Active Probes. *Journal of Micromechanics and Microengineering*, 18:1–11, 2008.

[44] O. Sarid. *Scanning Force Microscopy.* Oxford Universit Press, New York, 1991.

[45] E. Schaffer, T. Albrecht, T. Russell, and U. Steiner. Electrically Induced Structure Formation and Pattern Transfer. *Nature*, 403(6772):874–877, February 2000.

[46] M. Sitti. Survey of Nanomanipulation Systems. In *Proceedings of the 2001 1st IEEE conference on Nanotechnology*, pages 75–80, October 2001.

[47] M. Sitti. NSF Workshop on Future Directions in Nano-Scale Systems, Dynamics and Control. Technical report, Carnegie Mellon University, 2003.

[48] R. Stevens, C. Nguyen, and M. Meyyappan. Nanomanipulation and Fabricaiton by Ion Beam Molding. *IEEE Transactions on Nanotechnology*, 5(3):255–257, May 2006.

[49] T. Sulchek, S. C. Minne, J. D. Adams, D. A. Fletcher, A. Atalar, C. F. Quate, and D. M. Adderton. Dual Integrated Actuators for Extended Range High Speed Atomic Force Microscopy. *Applied Physics Letters*, 75(11):1637–1639, September 1999.

[50] R. Superfine, M. Falvo, R. Taylor, and S. Washburn. *Nanomanipulation: Buckling, Transport and Rolling at the Nanoscale.* CRC Handbook of Nanoscience, Engineering and Technology. CRC Press LLC, 2002.

[51] D. W. Trim. *Applied Partial Differential Equations.* PWS-KENT Publishing Company, 1990.

[52] Q. M. Yang and S. Jagannathan. Atomic Force Microscope-based Nanomanipulation with Drift Compensation. *International Journal of Nanotechnology*, 3(4):527–544, 2006.

[53] J. Zhang, N. Xi, G. Li ans H. Chan, and U. Wei. Adaptable End Effector for Atomic Force Microscopy Based Nanomanipulation. *IEEE Transactions on Nanotechnology*, 5(6):628–642, November 2006.

[54] W. M. Zhang, G. Meng, and H. G. Li. Adaptive Vibration Control of Micro-cantilever Beam with Piezoelectric Actuator in MEMS. *International Journal of Advanced Manufacturing Technology*, 28(3–4):321–327, 2006.